Spring 5-11-2019

VALIDATION OF THE STATE BASED PERIDYNAMIC LATTICE MODEL

Anima Bista

Anima Bista

Candidate

Civil Engineering

Department

This thesis is approved, and it is acceptable in quality and form for publication:

Approved by the Thesis Committee:

Dr. Walter Gerstle, Chairperson

Dr. Timothy Ross

Dr. Fernando Moreu

VALIDATION OF THE STATE BASED PERIDYNAMIC LATTICE MODEL

by

ANIMA BISTA

B.S., CIVIL ENGINEERING, TRIBHUVAN UNIVERSITY, NEPAL, 2015

THESIS

Submitted in Partial Fulfillment of the
Requirements for the Degree of

Master of Science
Civil Engineering

The University of New Mexico
Albuquerque, New Mexico

May 2019

DEDICATION

To my dear parents, Shobha and Homraj, my husband, Dibit and my brother Anish for their unconditional love and support!

ACKNOWLEDGEMENTS

I would like to thank my advisor Dr. Walter Gerstle for giving me his precious time and opportunity to work with him. It has been a wonderful learning experience for me. Prof. Gerstle's door were always open whenever I approached him with questions.

I would also like to thank my committee members Dr. Timothy Ross and Dr. Fernando Moreu for their time and support. I thank the Civil Engineering Department, University of New Mexico. I would also like to thank Center for Advanced Research Computing (CARC) for allowing me to use their high performance computers.

Finally, I would like to express my profound gratitude to my friends Siavash Nikravesh for his support in helping me getting familiar with peridynamics, and Hari K. Dhamala for his support during the laboratory experiments and writing of the laboratory report supporting my thesis. Thank you all!

VALIDATION OF THE STATE BASED PERIDYNAMIC LATTICE MODEL

By

ANIMA BISTA

B.S., CIVIL ENGINEERING, TRIBHUVAN UNIVERSITY, NEPAL, 2015

M.S., CIVIL ENGINEERING, UNIVERSITY OF NEW MEXICO, USA, 2019

ABSTRACT

This thesis presents a study performed to validate the State-based Peridynamic Lattice Model (SPLM) using results obtained from laboratory experiments. The SPLM is capable of modeling cracking of solids using particle lattices. We use a plane stress, elastic-plastic damage SPLM model for the simulations. The SPLM model is appropriate for computational simulations of cementitious materials as it automatically allows cracks to develop. In this study, the lattices are rotated through different angles and the variations of the cracking patterns are studied.

In the laboratory, we performed nine Brazilian split cylinder tests, three anchor pullout/direct tensile tests, and eight compression tests on cylinders of standard size. We also tested four beams as modulus of rupture tests. The results from the laboratory tests and the SPLM simulations were then compared. The comparison indicates that the SPLM produced similar results as the laboratory experiments and the ACI code predictions. These results indicate that SPLM is a reasonable simulation method for these types of specimens.

Keywords: SPLM, peridynamic, plane stress, crack, damage, plasticity.

Table of Contents

List of Figures

List of Tables

Chapter 1 Introduction

1.1 Motivation

Computers have drastically aided in the numerical analysis of structures. Numerous commercial and academic computer programs are available that use the Finite Element Method (FEM) for computation. Despite being the most common tool used, it is difficult to use the FEM to simulate structures that crack.

There have been numerous studies conducted in the past to model crack growth in plain and reinforced concrete. Various remeshing techniques and linear and non-linear models have been developed to simulate crack propagation. During World War II, when warships developed cracks, Linear Elastic Fracture Mechanics (LEFM) was developed and applied to study crack propagation (Shabazpanahi et. al, 2012). Later, LEFM was also used for studying cracks in concrete structures. However, LEFM was found to be unacceptable because concrete does not satisfy the assumptions of LEFM. The popular models for modeling cracks in concrete are the discrete crack model and the smeared crack model. Cervenka and Saouma (Cervenka & Saouma, 1995) have stated that the discrete crack model is not as mesh-sensitive as the smeared crack model, but requires remeshing at each crack increment. But often, the crack propagation is dynamic which increases the difficulty when using the discrete crack model. Peridynamics might be an effective solution to this problem as it allows the cracks to propagate under arbitrary dynamical loading conditions and no complicated meshing is required for the simulation.

The deformation field is not continuous in regions of damage and cracking. Continuum mechanics theory, therefore, is insufficient for crack analysis. We cannot apply the partial differential equations of classical mechanics directly on these cracks. An

alternative method of analysis is sought which reduces the complexity of the problem and helps find a solution that can be applied in regions of damage and cracking.

The peridynamic model was first developed by Silling (Silling, 2000) and it assumes Newton's second law applies to each differential volume in the domain of analysis (Gerstle, 2015). Silling renamed his first theory of peridynamics as "bond-based" and later developed "state-based" peridynamics. In peridynamics, a pairwise force function f is assumed to exist between each pair of particles which are closer together than the assumed material horizon, δ. When the pairwise force function is a function of the states of all the nearby particles, peridynamics is called "state-based" peridynamics (Silling et. al, 2007). In contrast, the bond-based peridynamic model assumes that the force between the two particles is only dependent on the states of the two interacting particles and does not depend upon the states of other nearby particles. The bond-based model was soon realized to be insufficient. Bond-based theory cannot model Poisson's ratio other than one-quarter for plane strain (or one-third for plane stress) and is incapable of modeling isochoric plastic deformation.

For state-based peridynamics, the pairwise force function may depend upon the relative reference and deformed locations of all the particles within the peridynamic horizon, as well as upon other variables such as damage and plastic stretch. The number of particles in the defined horizon is fixed. Gerstle (Gerstle, 2015) in 2015, developed the State-based Peridynamic Lattice Model (SPLM) which specializes the state-based peridynamic model. In the SPLM, the particle families are assumed invariant, which reduces the cost of computation.

1.2 Scope

The objective of this thesis is to compare SPLM computer simulations to laboratory experiments. While continuum mechanics considers the deformation field to be continuous, SPLM models the structure as a particle lattice. SPLM does not assume continuity, but the particles are also not random, as with the molecular dynamics model. The particles remain in the lattice and interact with the same set of particles throughout the simulation. This makes the model more understandable and computationally efficient.

In this thesis, we use the SPLM for the simulation of concrete specimens. SPLM has the potential to be used as a tool for simulating the concrete damage, using Poisson's ratios other than one-quarter (one-third) and modeling isochoric plastic deformations. We use an SPLM code developed in Fortran for the simulation, and the results are displayed using MATLAB. The code models elasticity, plasticity, and damage and we study the concrete behavior using SPLM. An initiative is taken to use the SPLM to model laboratory specimens and validate the results against laboratory experiments and ACI code predictions. SPLM simulations are performed for:

1. Brazilian split cylinder test;
2. Direct tension test;
3. Direct tension test with the embedded bolt;
4. Modulus of rupture test; and
5. Direct compression test.

We used standard laboratory models for both the laboratory experiments and the simulations, so the results can be easily compared.

1.3 Outline of Thesis

This thesis has six chapters.

Chapter One, Introduction, has introduced the motivation and the scope for the research.

Chapter Two, Literature Review, is the discussion of the history and the previous works in the field of solid mechanics. This includes the continuum model, the concepts of stress and strain, and fracture mechanics in brief. We discuss here how these concepts are difficult to implement digitally for the computer simulation.

Chapter Three explains the theory of peridynamics. Here, we discuss the peridynamic models and the SPLM model. An overview of the elastic, plastic and damage SPLM models are also discussed.

Chapter Four presents the laboratory experiments conducted for the four different strength tests. Three of them are tensile strength tests and one of them is a compressive strength test. A sieve analysis was also performed to observe the distribution of the aggregate based on size.

Chapter Five, SPLM Validation, describes the use SPLM to simulate the concrete models that were tested in the laboratory. The SPLM results are then compared with the laboratory experiments.

Chapter Six, Summary and Conclusions, summarizes and concludes the research conducted and suggests future work using SPLM.

Chapter 2 Literature Review

Concrete is a heterogeneous material that demonstrates quasi-brittle nature. It is a well-known fact that concrete is strong in compression and weak in tension. Concrete fails in tension at much lower loads than it fails in compression. Practical engineering seems to simply ignore the tensile strength of concrete and instead uses steel reinforcement to resist the tensile forces within the structure. Raphael (Raphael, 1984) mentions that it is not practical to reinforce a large structure, like a dam, with a huge quantity of steel, and hence the tensile strength of concrete has to be taken into account. This is one reason why the tensile strength of concrete is important and cannot be ignored. Concrete structures would reduce to a heap of rubble if there were no tensile strength to hold them together.

There have been numerous efforts to determine the tensile strength of concrete. Different tests have been conducted in the laboratory with a variety of specimen configurations, to determine the tensile strength of concrete. The development of fracture mechanics and numerical simulations have aided in the process. We can now apply numerous cracking models using fracture mechanics concepts to determine damage and cracking.

When concrete fails in tension after reaching the ultimate tensile strength, cracks are formed as damage coalesces. The initiation and growth of cracks are beyond the scope of classical mechanics. Therefore, fracture mechanics was developed to accurately predict the crack formation and propagation. Early fracture mechanics assumed a linear elastic approach which was later found to be inappropriate for concrete structures. Several models and theories have been developed to portray crack propagation in concrete.

2.1 History of Fracture Mechanics Theory

Various models and theories have been developed that have contributed to the advancement of fracture mechanics. Fracture mechanics developed rapidly during World War II when warships started cracking and linear elastic fracture mechanics was developed. Progressively, we will discuss some of the crack models in this section.

2.1.1 Inglis infinite plate theory

When Inglis (Inglis, 1913) found the solution to Navier-Cauchy's stress theory for an elliptical hole in the infinite plate shown in Fig. 2-1, he observed that the maximum tensile stress occurs in the boundary of the hole, on the major ellipse axis. The maximum tensile stress is perpendicular to the major axis, and is given by,

$$\sigma_{max} = \sigma_0(1 + 2\sqrt{\frac{a}{\rho_c}}) \tag{2.1}$$

where a and b are the radii of the ellipse along x and y-axis respectively, σ_0 is the applied stress, σ_{max} is the maximum normal stress and $\rho_c = \frac{b^2}{a}$ is the radius of curvature of the ellipse on the major axis. When the ellipse narrows, the crack becomes very sharp and the maximum stress becomes infinite. The Eq. 2.1 then becomes

$$\frac{\sigma_{max}}{\sigma_0} = \infty. \tag{2.2}$$

This made the classical stress approach impossible to apply to cracks, where b goes to zero, as singularity in stress results. Infinite stress cannot be compared to a finite strength. Therefore, Griffith developed an energy-balance approach to predict crack growth, as described next.

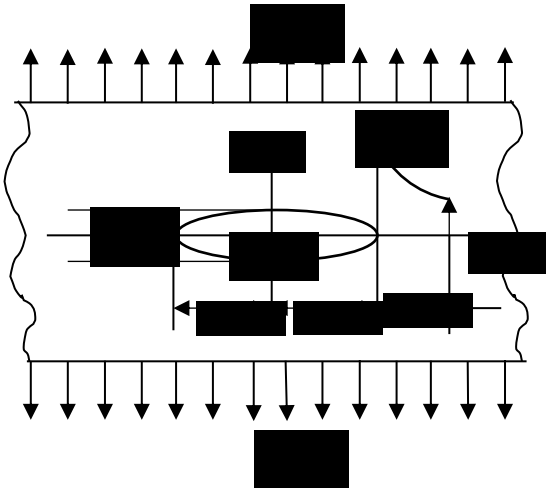

Figure 2-1 Inglis infinite plate with elliptical hole, showing σ in front of crack

2.1.2 Griffith's energy criterion and Irwin's stress intensity factor approach

Griffith (Griffith, 1921) in 1921, developed an approach which introduced an energy balance concept in LEFM. When the stress at the crack tip becomes infinite, as described in the work done by Inglis, an alternative to the stress concept must be developed. Griffith developed the "Griffith's energy criterion" that describes crack propagation. After performing various tests using glass rods and fibers, Griffith observed that the presence of flaws or scratches on the glass surface led to decreased strength. This led him to develop an energy approach, which assumes that a certain amount of energy is required to form a new crack surface. When the crack propagates, potential energy is released, and it is used to break the bonds at the crack tip. The law of conservation of energy must be satisfied. According to him, when the rate of change (decrease) of potential energy G exceeds a certain value G_F, the crack acquires enough energy to propagate, if $G \geq G_F$, crack will propagate. Griffith's criterion is valid for truly brittle materials like glass rods. For concrete, which is quasi-brittle, and steel which is ductile, Griffith's energy criterion is insufficient. Steel and concrete undergo plastic deformation which needs to be considered

in the energy balance. Irwin, in 1957, developed the stress intensity factor approach, that added the energy of the plastic work to the Griffith's existing surface energy to give the critical fracture energy.

$$G_F = G_{surface} + G_{plasticity} \tag{2.3}$$

In the stress intensity factor approach, the normal stress in front of the crack tip is infinite, following the expression $\sigma = \frac{K}{\sqrt{2\pi r}}$ where, r is the distance in front of the crack tip and K is the stress intensity factor (Hillerborg, Modéer, & Petersson, 1976). Cracks grow when K is critical, i.e. $K = K_C$, where K_C is the fracture toughness. This approach is applicable only for the crack propagation and does not explain the crack formation. The relationship between critical fracture energy and critical stress intensity factor for planar problems is given by,

$$G_C = \frac{{K_C}^2}{E'} \tag{2.4}$$

where E'=E for plane stress and $E'= E/(1-\upsilon^2)$ for plane strain, E is Young's modulus and υ is Poisson' s ratio.

2.2 Nonlinear fracture mechanics

The Fracture Process Zone (FPZ) is the zone near the crack tip where irreversible damage and plasticity occurs. When the fracture process zone is of significant size with respect to the specimen size, the fracture process zone must be modeled in some ways. If the FPZ is explicitly modeled, the theory is called "nonlinear fracture mechanics".

2.2.1 Cohesive crack model

The cohesive crack model was the earliest of the nonlinear fracture mechanics models. The earliest cohesive crack models were developed during the 1960s by Dugdale (Dugdale, 1960) and Barenblatt (Barenblatt, 1962). The models developed assumed a preexisting crack, and only explained its growth. These models were not sufficient to explain the initiation of the cracks. Hillerborg (Hillerborg et al., 1976) in 1976 developed the model shown in Fig. 2-2, which not only explained the growth of existing cracks but also explained the formation of new cracks. Hillerborg et. al. used the assumption that cracks form when the stress reaches a critical tensile stress, f_t. The model is defined for the opening mode I but can be extended to modes II and III. The model was initially named the "fictitious crack model" however, it is widely known as the cohesive crack model today, and it is very much like Barenblatt's cohesive crack model.

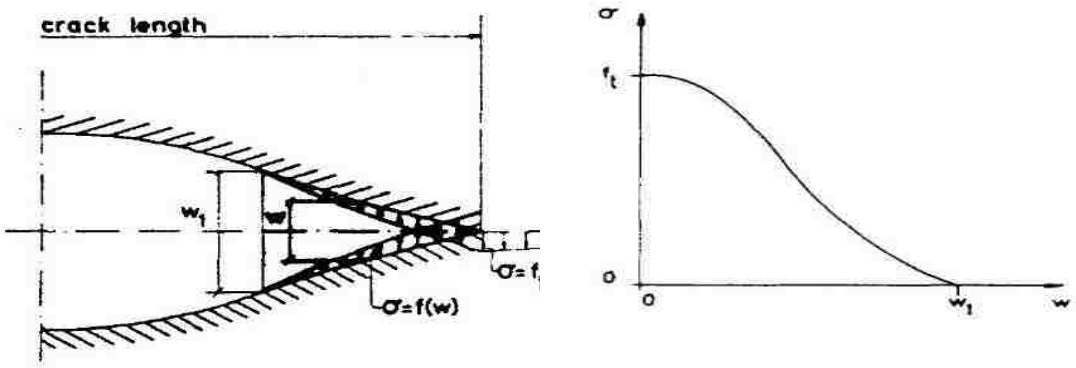

a) Crack model demonstrating crack length and maximum stress b) Stress versus COD diagram

Figure 2-2 Hillerborg's fictitious crack model (Hillerborg et al., 1976)

In the graph in Fig. 2-2 b), we can see that when the crack width w equals 0, the stress is f_t which means the crack has just started to form. Once the crack starts to open, the stress decreases; however, it does not suddenly go to zero. The stress decreases with the increase in crack width until w equals w_1 at which value the stress goes to zero. Hence, the

cohesive traction is a function of the crack opening displacement. The fracture energy is given by

$$\int_0^{w_1} \sigma(w)dw = G_F \,, \tag{2.5}$$

where G_F is the fracture energy and $\sigma(w)$ is the cohesive stress function. The model produces better results for concrete than LEFM but is more difficult to implement on a computer.

2.2.2 Interface element approach

The interface element approach is a way to implement the fictitious crack model numerically. Gerstle et. al. (Gerstle & Xie, 1992) have demonstrated how the Hillerborg's fictitious crack model can be implemented by introducing interface elements along the crack. There have also been other implementations of the interface element model.

2.2.3 Bond-slip model

A bond slip model is necessary for simulating reinforced concrete. Ingraffea and coworkers (Ingraffea et. al, 1984) studied the secondary cracks that emerge when the primary crack crosses the reinforcing bar in the model. A special version of interface element called the "tension-softening" element is introduced at the crack crossing to analyze the nonlinear behavior caused by the bond slip between the bar and the concrete.

2.3 Computational fracture mechanics

The nonlinear fracture mechanics models were the milestones in predicting that not all the materials follow linear elastic fracture mechanics. However, these methods were difficult and required a great amount of time and effort to computationally implement. Computational fracture mechanics became more popular with advancements in technology. There are three basic computational fracture mechanics models:

1) discrete crack models,
2) smeared crack models, and
3) lattice and particle models.

Discrete crack propagation considers the crack as a geometrical feature, rather than as a material property. Discrete crack modelling involves continuous remeshing of the crack topology as the crack front propagates. The difficulty with this model is the large effort required for remeshing every time the crack propagates. With new computational techniques, automatic mesh regeneration can be done to change the mesh topology. Gerstle et. al. (Gerstle & Xie, 1992) have used a simple fictitious crack model to demonstrate the cohesive discrete crack propagation method. The method includes the use of interface elements to represent the crack growth.

Although discrete crack models seem to be a better computational approach than smeared crack models for many problems, there are certain limitations. It is difficult to model multiple cracks and intersecting cracks which in addition creates problems for mesh convergence studies (Gerstle, 2015).

The smeared crack model can model diffuse (multiple) cracks following the concept of continuum damage mechanics. The smeared crack results from the assumption that the material body is a continuum. However, the material body has a complex internal structure and needs discretization. In smeared crack modelling, the crack is simulated as the material stiffness decreases as damage occurs. Increasing strain causes a decrease in stress in the strain-softening model. Strain-softening considers the material to be unstable which violates the Drucker's stability postulates (Bažant & Jirásek, 2002). The instability of the material causes the strain to localize to zero volume and the fracture energy to

diminish to zero. To prevent the strain localization, which causes mesh sensitivity during the finite element analysis, non-local effects must be considered. The localization limiter has been implemented in the finite element analysis for non-local damage modeling. According to this concept, the stress at a point is not only dependent on the strain at that point, but also on the average strain of all the neighboring points within a finite domain. However, fine meshing is required in the region of damage in this neighborhood, creating problems in conducting convergence studies.

The particle method and the lattice model are closely related to each other. In the particle method, the interactions of the particles are defined in the model. The particle configuration changes under the application of load. The particle motion is governed by Newton's laws (Wittel, Kun, & Herrmann).

In early lattice model simulations, truss elements were assumed to connect the nodes. When the truss forces reached critical values, the truss was removed from the lattice. The peridynamic model provides a more fundamental and accurate approach. We discuss peridynamics in detail in the next chapter.

2.4 Theory of Elasticity

The theory of elasticity is the simplest theory of the deformation of solids. The modern theory of elasticity and its discovery dates to the 1820s, when Navier and Cauchy introduced the concepts of stress and strain.

Consider two points at reference (undeformed) locations in an elastic body as shown in Fig. 2-3. Point **P** is at location (X,Y,Z) and point $\mathbf{P}'$ is at (X',Y' and Z'). These points are the position vectors relative to the origin of co-ordinate system X,Y,Z. The relative position vector between these two points is given by $\mathbf{R} \equiv \mathbf{P}' - \mathbf{P}$. When

deformation occurs, these points move to **p** and **p'** respectively. The displacement of **P** to **p** is given by vector **U,** and the displacement of **P'** to **p'** is given by **U'**.

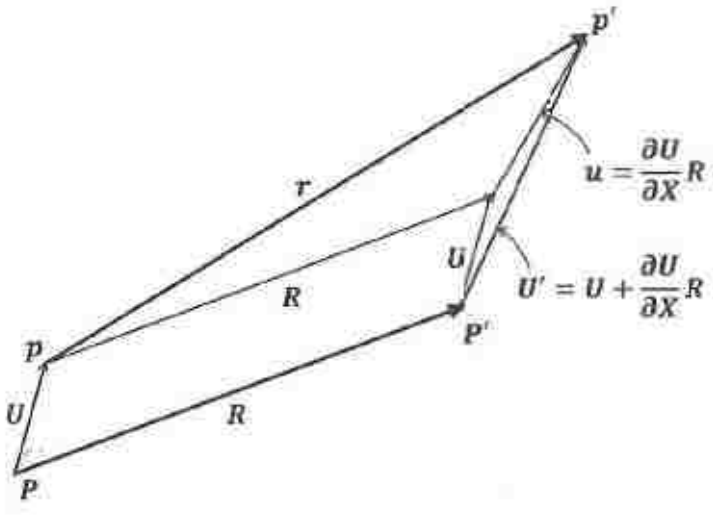

Figure 2-3 Updated Navier's theory of elasticity (Gerstle, 2015, pp-57)

We now refer to (Gerstle, 2015) to follow Navier's theory and determine the bond force between the particles. The displacement field is demonstrated using a Taylor series expansion,

$$U'_i = U_i + \sum_{j=1:3} \frac{\partial U_i}{\partial X_j} R_j + O(R^{2}), \quad \text{or} \tag{2.6}$$

$$\boldsymbol{U'} \cong \boldsymbol{U} + \frac{\partial \boldsymbol{U}}{\partial \boldsymbol{X}} \boldsymbol{R}.$$

The linearized relative displacement vector u is given by

$$\mathbf{u} = \mathbf{U'} - \mathbf{U} = \frac{\partial \boldsymbol{U}}{\partial \boldsymbol{X}} \boldsymbol{R}. \tag{2.7}$$

The magnitude of **u** has to be small relative to **R** for the above equation to be valid. However, this linearized relative displacement **u** is not the change in bond length of **R**. The change in bond length is given by the projection of **u** in the direction of **R,** rather than **u** itself. The notational representation of this change in length is given as

$$\Delta R = \frac{(U_{i,k}\, R_k)R_i}{\sqrt{R_j R_j}} \tag{2.8}$$

The bond force is assumed to be proportional to the change in length ΔR between the particles located at the deformed positions **p** and **p'**. The bond force acts per unit volume and is given by

$$F = G(R)\Delta R dV', \tag{2.9}$$

where dV' is the differential volume associated with **p'** and G(R) is a rapidly decaying function of R = ||**R**||. The only parameter used in the Navier's theory is ε which represents the integral used in the derivation of virtual work done by bonds. The internal virtual work done by bonds going through elongation ΔR is

$$\delta W_{bond} = \delta\Delta R \bullet F = \frac{1}{2}\delta(\Delta R^2)G(R)dV' \tag{2.10}$$

where, $\frac{1}{2}$ is included because each bond is shared by two particles. Now integrating the virtual work given by Eq. 2.10 over the spatial domain and then in Cartesian and spherical domain, we obtain

$$\delta W_{bond\_all} = \frac{1}{2}\varepsilon\delta[3U_{1,1}{}^2 + \left(U_{1,2} + U_{2,1}\right)^2 + 2U_{1,1}U_{2,2} + \left(U_{1,3} + U_{3,1}\right)^2 + 2U_{1,1}U_{3,3} + 3U_{2,2}{}^2 + \left(U_{2,3} + U_{3,2}\right)^2 + 2U_{2,2}U_{3,3} + 3U_{3,3}{}^2$$

where ε is,

$$\varepsilon \equiv \left(\frac{2\pi}{15}\right)\int_0^\infty R^4\, G(R)dR. \tag{2.11}$$

Navier then assumes body forces **B** and surface tractions **T**. For a body to be in equilibrium, the total virtual work done by all forces must be zero. However, Cauchy argued (correctly) that Navier's theory is insufficient to fully define elasticity. He introduced the concepts of stress and strain and the partial differential equations of linear elasticity, valid in a continuum. Cauchy built upon the work of Navier to develop the

Navier-Cauchy equations of elasticity. Cauchy's concept of stress and strain are discussed in the next section.

2.5 Continuum Mechanics

In order to appreciate SPLM, one must first fully understand continuum mechanics. Continuum mechanics is one model for the mechanical behavior of the solids and the fluids. The material is modelled in a continuum space rather than as discrete particles. Continuum mechanics follows the fundamental principles of conservation of mass, energy, and momentum (Mase & Mase, 1999). Continuum mechanics quantities are mathematically represented as vectors and tensors for simplicity. The physical and the geometrical quantities used in continuum mechanics are represented as tensors. The physical continuum space is represented by Cartesian coordinate axes, as shown in Fig. 2-4.

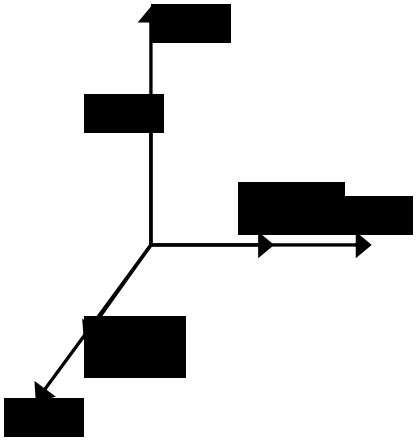

Figure 2-4 Cartesian coordinate system and unit Vector

2.6 Traction Vectors and Stress Tensors

The traction vector **t** is the force **ΔF** acting on a cross-sectional area ΔA divided by that area of cross-section in the limit, as ΔA goes to zero. It has the units of stress.

$$\boldsymbol{t} = \lim_{\Delta A \to 0} \left(\frac{\Delta \boldsymbol{F}}{\Delta A}\right) \tag{2.12}$$

However, this definition is only valid if the surface, where the traction is defined, is continuous. If there is any kind of discontinuity present in the surface, the above definition will not suffice or requires more assumptions which limits its use.

The traction acting upon the two sides of the plane and passing through a point are equal in magnitude but opposite in direction. Cauchy has proved this by assuming two planes to pass through the top and bottom of a cylinder (Koenemann, 2014). Letting the height of cylinder vanish, we will see that traction on two faces of the cylinder will be equal in magnitude and opposite in directions. This is more clearly explained in (Gerstle, 2015). In continuum mechanics, the equation of conservation of linear momentum is given by

$$\int_B \rho \ddot{\boldsymbol{x}}\, dV = \int_B \rho \boldsymbol{b} dV + \int_{\delta B} \boldsymbol{t} dA, \tag{2.13}$$

where **B** is the deformed volumetric domain of the body, ρ is the density of differential volume dV, $\ddot{\boldsymbol{x}}$ is the acceleration of the particle, **b** is the applied body force per unit mass, δB is the surface of the domain B, and **t** is the applied traction on the deformed area dA. So, if we let the height of the cylinder vanish, the volume and the curved area of the cylinder, shown in Fig. 2-6 decreases to zero. Then from Eq. 2.13,

$$\int_B \rho \ddot{\boldsymbol{x}}\, dV = \int_B \rho \boldsymbol{b} dV + \int_{\delta P cyl} \boldsymbol{t} dA + \int_{\delta P+} \boldsymbol{t} dA + \int_{\delta P-} \boldsymbol{t} dA, \tag{2.14}$$

or,

$$0 = 0 + 0 + \int_{\delta P+} \boldsymbol{t} dA + \int_{\delta P-} \boldsymbol{t} dA$$

Thus, the traction on opposite sides are equal in magnitude but opposite in direction. This can also be derived from Newton's third law of motion.

$$\boldsymbol{t}(x, n) = -\boldsymbol{t}(x, n), \tag{2.15}$$

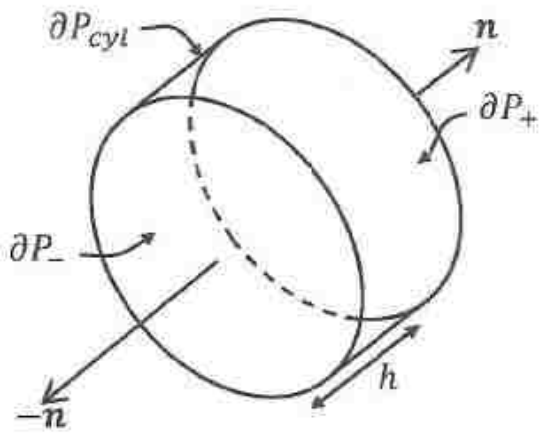

Figure 2-5 Cylindrical body (Gerstle, 2015)

2.7 Cauchy's Stress Theory

Simplest stress tensor is named after Cauchy and is known as Cauchy's stress tensor and is a second order tensor. If we take the traction vector described in Eq. 2.12, acting at a point in a surface, it can be decomposed into two components $\Delta\sigma^{avg}_S$ and $\Delta\sigma^{avg}_N$ which are the average stresses acting tangential and normal over the area ΔA respectively (Khraisi & Shen, 2012). When the area shrinks infinitesimally, the stresses are then defined for a point over the limit given by,

$$\sigma_S = \lim_{\Delta A \to 0} \left(\frac{\Delta F_S}{\Delta A}\right) \quad , \quad \sigma_N = \lim_{\Delta A \to 0} \left(\frac{\Delta F_N}{\Delta A}\right).$$

The tangential force ΔF_S further has two orthogonal components, one in-plane and another out-of-plane named as ΔF_{S1} and ΔF_{S2} respectively. This way, there are three stresses acting at a plane in a body. Similarly, a cubic volume is defined by six such faces shown in Fig. 2-6.

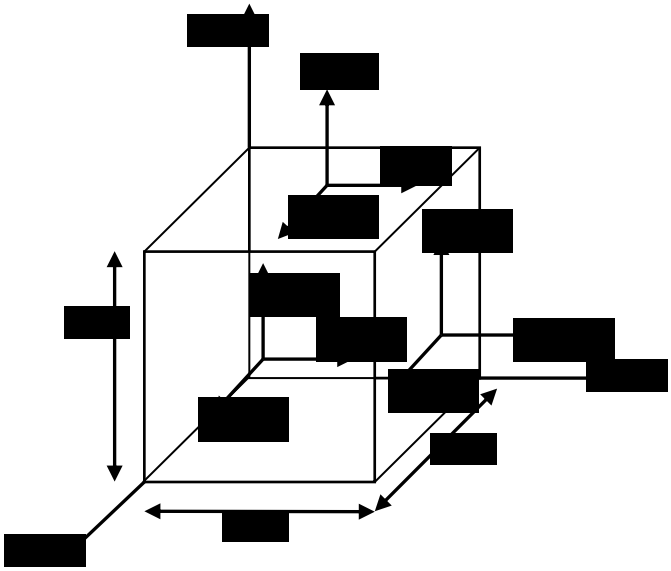

Figure 2-6 Components of Cauchy's stress tensor

We thus have three stresses on each of the surfaces. It is assumed that the volume of the cube is infinitesimally small i.e. dx, dy, and dz tend to zero, shrinking the cube to a point. The cube is placed in such a way that the normal of each face aligns with the unit vectors of Cartesian coordinate system shown in Fig. 2-6. It is noticed that the plane surfaces opposite to each other have equal and opposite stresses as shown in Eq. 2.15. This leaves us with 9 independent stress components. Further, for a cube dx=dy=dz and we assume an equilibrium condition for which our sum of moments equal zero. Hence our stress tensor is symmetric,

$$\sigma_{xy} = \sigma_{yx}, \qquad \sigma_{yz} = \sigma_{zy}, \qquad \sigma_{xz} = \sigma_{zx}.$$

Thus, we have six independent Cauchy's stress components, which are generally represented as σ_{ij}, where i is the direction and j is the plane along which the stresses act. The planes can be arbitrary or oblique and a stress transformation is done to obtain stress components. Mohr's circle method is a graphical representation of stress transformation in two-dimensional problems. Cauchy's stress tensor can be further decomposed into volume

and deviatoric components according to the requirements. A detailed derivation can be found in (Khraisi & Shen, 2012). Cauchy's stress tensor is used for material bodies experiencing small deformations. For the larger deformations, the first and second Piola-Kirchoff's stress tensor may be used. The finite element method can analyze larger deformations using these tensors. A more detailed explanation on Piola-Kirchoff's stress tensor is found in (Gerstle, 2015). However, this method is difficult to use and apply. That is why a need for a different approach was felt which did not involve the continuous concepts of stress and strain.

2.7.1 Limitations of Cauchy's Stress Theory

Cauchy's stress theory has been in use ever since it was discovered and most of the modern theories in solid mechanics today have been derived based on Cauchy's stress tensor. There are however, certain limitations of Cauchy's theory which have been either ignored or never brought to light. Cauchy's stress theory is derived assuming a spatial continuum and does not have a clear explanation to what changes will there be when cracks develop. The boundary conditions, although mentioned, are ambiguous in Cauchy's theory (Koenemann, 2014). It is difficult to study the post-peak behavior of real materials after the crack occurs, as the material is no longer continuous in the cracking region. Hence, the need for peridynamics, presented in the next chapter.

Chapter 3 Peridynamics

Peridynamics was first developed by Stewart Silling in 2000 (Silling, 2000). Peridynamics is derived from the Greek words Peri meaning *near* and dynamics meaning *force* (Silling, 2000). The smeared and the discrete crack models discussed in Chapter 2, literature review, are not satisfactory for modelling concrete structures. Cracks are naturally formed discontinuities and they should be allowed to evolve naturally during the simulation. Peridynamics allows damage and cracks to form naturally without the problems associated with continuum methods.

The continuum theory of peridynamics is based upon the fact that Newton's second law holds true for every infinitesimal particle. Assume that a small particle P_i, has a mass dm_i, having undeformed position $\mathbf{X_i}$ and a displacement $\mathbf{u_i}$ within a domain R. The internal force **L** acting upon the particle is the internal of all bond forces acting upon the particle and is given by (Silling, 2000),

$$\boldsymbol{L}(X,t) = \int_R \boldsymbol{f}(\boldsymbol{u}(X',t) - \boldsymbol{u}(x,t), \boldsymbol{X'} - \boldsymbol{X}) dV_{X'} \tag{3.1}$$

where R is the reference space of the function. **L** has the unit of force per unit volume, and $\boldsymbol{f}$ has the units of force per unit volume squared.

Mathematically, Newton's second law of motion applied to this particle can be represented as:

$$(dm_i)\ddot{\boldsymbol{u}}_{\boldsymbol{i}} = d\boldsymbol{F}, \tag{3.2}$$

where, $\ddot{\boldsymbol{u}}_{\boldsymbol{i}}$ is the acceleration of the particle and $d\boldsymbol{F}$ is the force vector acting upon the particle.

Dividing Eq. 3.2 on both sides by differential volume dV_i, we get the following:

$$\rho\ddot{\boldsymbol{u}}_{\boldsymbol{i}} = \boldsymbol{L} + \boldsymbol{b} \tag{3.3}$$

This is the peridynamic equation of motion where ρ is mass density, and **L** and **b** are the internal force and the externally-applied body force per unit volume, respectively (Gerstle & Sau, 2004). Substituting the value of **L** from Eq. 3.1 onto Eq. 3.3 gives

$$\rho \ddot{\boldsymbol{u}}_{\boldsymbol{i}} = \int_R \boldsymbol{f}(\boldsymbol{u}(\boldsymbol{X}', t) - \boldsymbol{u}(\boldsymbol{X}, t), \boldsymbol{X}' - \boldsymbol{X}) dV_{X'} + \boldsymbol{b}. \quad (3.4)$$

The function $\boldsymbol{f}(\boldsymbol{u}(\boldsymbol{X}', t) - \boldsymbol{u}(\boldsymbol{X}, t), \boldsymbol{X}' - \boldsymbol{X})$ is called the pairwise force function and has units of force per volume squared. The function $\boldsymbol{f}$ may also be a function of damage and plastic deformation.

The peridynamic constitutive model is defined by the forces between particles. The force acting upon the particle $\mathbf{P_i}$ is a function of reference location $\mathbf{X_j}$ and the location after deformation $\mathbf{x_j}$ of the nearby particle $\mathbf{P_j}$ with respect to the reference location $\mathbf{X_i}$ and deformed location $\mathbf{x_i}$ of particle $\mathbf{P_i}$. This force function $\boldsymbol{f}$ between the particles is also called the "pairwise force function".

The continuum peridynamic model uses the concept of force states and deformation states, in contrast to continuum mechanics, which uses the concepts of stress and strain (Gerstle & Soto, 2004). Peridynamics theory is different than the continuum mechanics theory by allowing the analysis of discontinuous deformations associated with cracks.

3.1 Bond-based Peridynamics

Silling's bond-based peridynamics assumes that the force between two particles is a function only of the reference and deformed positions of the two interacting particles and not dependent upon other neighboring particles. Silling later found bond-based theory to be insufficient to capture the observed material behavior, and so he developed the state-based theory. Bond-based and the state-based theory both employ the spatial continuum approach, however, the state-based theory makes the pairwise force function depend not

only upon the states of the two interacting particles, but also of other neighboring particles. State-based computational cost is higher than the bond-based computational cost, as the state-based model must compute the force function of many more neighboring particles.

Consider two particles at reference (undeformed) locations in a body, particle **P** at location **X** and particle **P'** at **X'** as shown in Fig. 3-1. When the deformation occurs due to the applied load, these particles move to new locations **x** and **x'** respectively. The vector from **X** to **X'** is given by ξ which we call the reference bond. The displacement of **P** is given by vector **u= x-X** and the displacement of **P'** is given by **u'= x'-X'**. The vector $\xi+\eta$ in Fig. 3-1 is called the deformed bond. The pairwise force function ***f*** in Eq. 3.4 describes the material behavior. In bond-based peridynamics, the force acting between the two particles is determined by the reference and the deformed locations of the interacting particles.

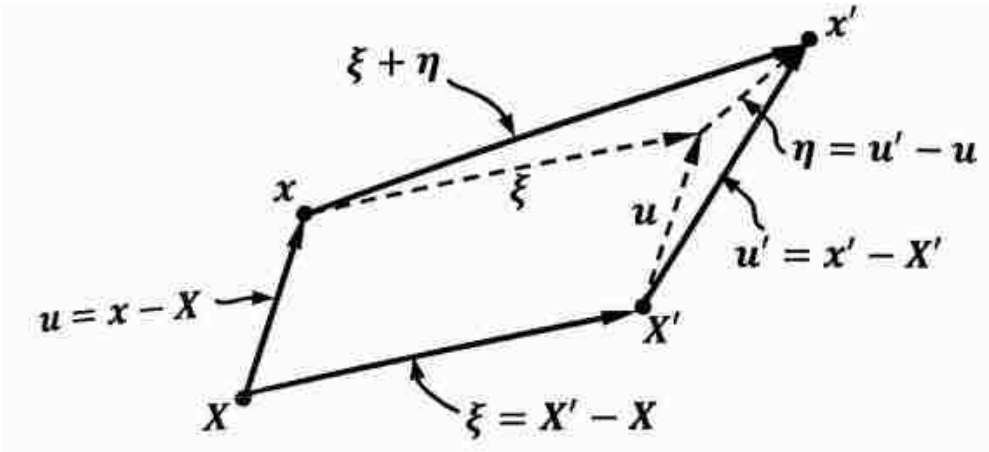

Figure 3-1 Kinematics of two nearby particles (Gerstle, 2015, pp-149)

When the peridynamic forces acting between the two particles are equal, opposite, and collinear with the deformed location, this is called "ordinary peridynamics". This is shown in Fig. 3-2.

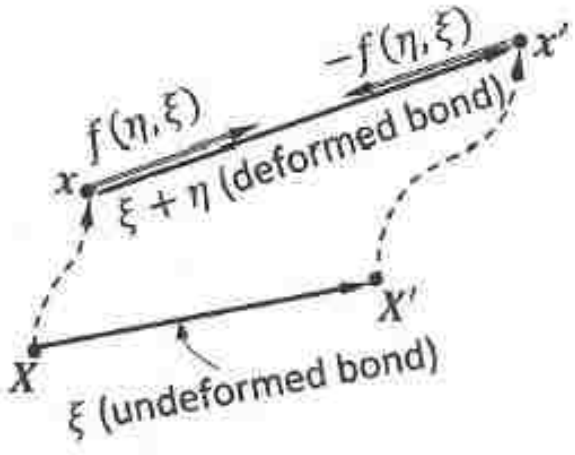

Figure 3-2 Ordinary bond-based peridynamic pairwise function ***f*** (Gerstle, 2015)

The ordinary bond-based peridynamic model is insufficiently general as it is not able to model materials with arbitrary Poisson's ratios. This problem can be corrected using the bond-based micropolar peridynamic theory, described next.

3.2 Bond-based Micropolar Peridynamic Theory

The Micropolar Peridynamic Lattice model (MPLM) was introduced by Gerstle et. al. (Gerstle, Sau, & Silling, 2007), who have completely discarded the continuum method and have adopted the discrete particle lattice model. In this micropolar model, the particles have the rotational degrees of freedom and associated. The micropolar model has the advantage over bond-based theory because it allows materials with arbitrary values of Poison's ratio to be simulated. More details about the micropolar peridynamic theory can be found in (Gerstle, Sau, & Aguilera, 2007) and (Honarvar, Gerstle, & Asadollahi, 2013). However, the MPLM is bond-based and is insufficient to model isochoric plasticity.

3.3 State-Based Peridynamic Model

When Silling found that his bond-based peridynamic theory was insufficiently general, he reformulated an improved theory called the state-based theory (Silling et al., 2007). In the bond-based theory, the damage, plasticity and the deformation of only two

particles are considered as inputs to the pairwise force function, whereas in the state-based theory the pairwise force function depends upon all particle states within the material horizon. The state-based model is able to model isochoric plasticity, as the function $\boldsymbol{f}$ accounts for all of the neighboring particles. It is also able to model the non-linear elasticity and large geometrical motions and allows dynamic particle motion.

Gerstle in 2015 replaced the real Euclidean material reference space with a lattice body and the vector ξ defining the reference bond with bond $\mathbf{B_j}$ in the lattice model. The domain defined by material horizon $\mathbf{H}$ is modified to the bond list $\mathbb{B}$. The peridynamic models developed by Silling and his colleagues still follow the continuum theory, while Gerstle has presented the state-based peridynamic lattice model (SPLM) (Gerstle, 2015). We can directly implement the SPLM for the computer without further discretization.

3.4 State-based Peridynamic Lattice Model (SPLM)

To begin with, we discard the continuum model of the solid and instead employ a particle lattice to represent the material. The particles in the lattice interact with each other. The SPLM is different than Silling's state-based continuum peridynamic model as SPLM uses a finite number of particles arranged in a lattice rather than an infinite number of particles in a continuum.

Consider the lattice body $£_R$, which contains the particles in a subset along with the null-particles. The positions of these particles are defined by the lattice vectors $\mathbf{b_i}$. These vectors correspond to the unit vectors $\mathbf{\hat{e}_j}$ in the Cartesian coordinate system defined in the Euclidean plane. Let $[B^N]$ be the N-dimensional lattice basis matrix which has components of the lattice basis vector $\mathbf{b_i}$:

Hence, $[B^N] = \begin{bmatrix} b_{11} & \cdots & b_{N_R 1} \\ \vdots & \ddots & \vdots \\ b_{1N_R} & \cdots & b_{N_R} b_{N_R} \end{bmatrix}$ so that, $\{\mathbf{X}\} = [B^N]\{a_i\}+\{\mathbf{X_0}\}$, where $\{X\}$ is the reference position of lattice particle $\{a_i\}$, and $\{\mathbf{X_0}\}$ is the position of the lattice particle. $\{a_i\}$ gives the integer lattice coordinates of each particle. The expression can also be written as,

$$\lfloor \mathbf{X} \rfloor = \lfloor a_i \rfloor \left\lfloor B_i^N \right\rfloor + \lfloor \mathbf{X_0} \rfloor.$$

3.4.1 3D Particle Configuration

The particle lattice can be arranged in many ways. The two main forms of arrangement of particles in a 3D lattice are: hexagonal closed pack (HCP) and face-centered cubic (FCC). These can be seen in Fig. 3-3.

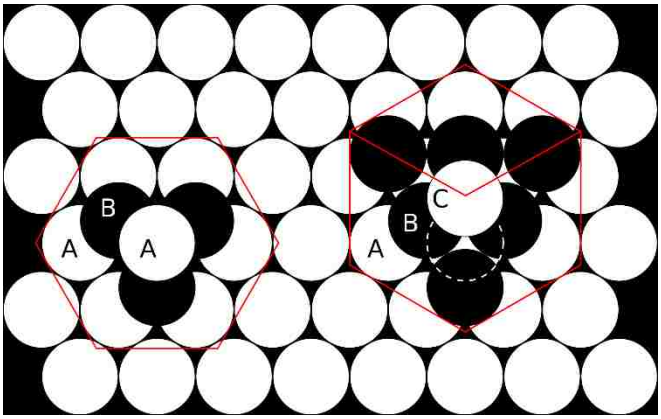

Figure 3-3 Hexagonal close-packed (left) and face-centered cubic (right) configurations https://sites.google.com/a/hartdistrict.org/ms-smith/home/modern-solid-materials/chapter-11 intermolecular -forces-and-liquids-and-solids/11-4-crystal-structure

Fig. 3-3, the stride given by the different labels is constant in the FCC configuration, hence, it is a true lattice. For FCC lattice if $N_R = 1$ then, it is one dimensional lattice and the lattice base matrix is given by $[B^1] = \mathbf{L}$ [1], where L is the lattice spacing. The lattice is unbounded and represented by the reference position vector $\mathbf{X_{ij}}$.

Hence, $\{\mathbf{X}\} = [B^N]\{a_i\}+\{\mathbf{X_0}\}$. For two-dimensional lattice, $[B^2] = \mathbf{L}[Q]\begin{bmatrix}1 & 1/2\\ 0 & \sqrt{3}/2\end{bmatrix}$ and for three dimensional lattice, $[B^3] = \mathbf{L}[Q]\begin{bmatrix}1 & 1/2 & 1/2\\ 0 & \sqrt{3}/2 & 1/2\sqrt{3}\\ 0 & 0 & 1/2\sqrt{3}\end{bmatrix}$ where **L** is the lattice particle spacing and [Q] is the lattice rotation matrix.

So, $\lfloor \mathbf{X_1}, \mathbf{X_2} \rfloor = \lfloor \mathbf{a_1}, \mathbf{a_2} \rfloor [Q] \begin{bmatrix}1 & \frac{1}{2}\\ 0 & \frac{\sqrt{3}}{2}\end{bmatrix} \lfloor \mathbf{X_{1_0}}, \mathbf{X_{2_0}} \rfloor$. Once the particles are arranged in the lattice with a given rotation [Q] and lattice origin $\lfloor \mathbf{X_0} \rfloor$, the model is ready for peridynamic simulation. The modeler must also choose which particles are "in" the body. Different lattice bodies having different dimensionality and located in different lattice configurations can be combined to create a structure. The tension specimen with the bolt is an example of a multibody structure. Different material bodies may have differing lattice spacings, lattice origins and lattice rotations. They are linked with each other using inter-body peridynamic forces.

The arrangement of particles with their neighboring particles forms a topology in a lattice. Lattice topology is helpful in defining the bond symmetry as well as which particles are the nearest to a reference particle and which are the second nearest, etc. A 3D particle has eighteen neighboring particles, twelve being the first nearest with the bond length L and six being the second nearest with bond length $\sqrt{2}L$, as shown in Fig. 3-4.

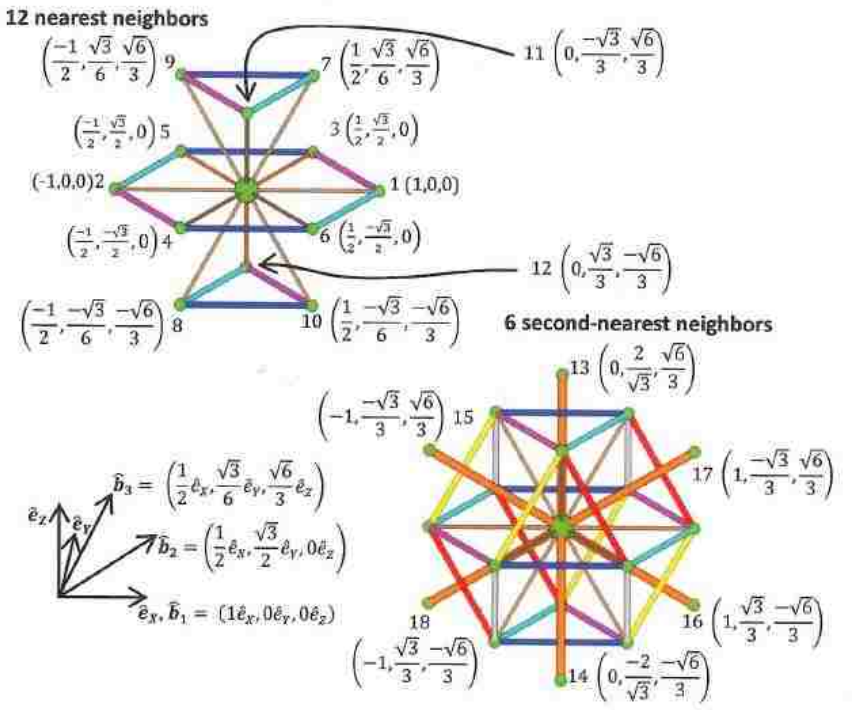

Figure 3-4 Bond numbering order of first and second nearest numbers for FCC lattice (Gerstle, 2015)

A particle is connected to adjacent particles by bonds B_j. The list of all these bonds through which the particle interacts with its adjacent particle is called the bond list. The absence of a bond is indicated by setting the neighbor bond list $N[P_i]<B_j> = P_\phi$ where P_ϕ is the null particle. Thus, using the lattice model, the simulation can be performed more systematically than if the particles are simply a random configuration of particles.

3.4.2 Elastic SPLM

In this subsection, consider the linear elastic SPLM bond force versus stretch relationship. A bond stretch causes a linearly related peridynamic bond force.

Let us assume the bond force matrix is defined as {F}. The stretch matrix is defined by {S}, and the relationship between the two is given by

$$\{F\} = [K]\{S\} \tag{3.5}$$

where [K] is similar to the stiffness matrix as defined in classical elastic mechanics. We now follow (Gerstle, 2015) for three-dimensional derivations, and derive the two-dimensional plane stress-strain case used in this thesis. For a 2D particle P_i, the stretch matrix is given by

$$\{S\}_i \equiv \begin{Bmatrix} S_1 \\ \vdots \\ S_j \\ \vdots \\ S_6 \end{Bmatrix}. \tag{3.6}$$

Each component of the stretch matrix is given by

$$S_j \equiv \frac{|deformed\ bond| - |reference\ bond|}{|reference\ bond|} \quad \text{or}$$

$$S_j \equiv \frac{L^* - L_0}{L_0}, \text{ where} \tag{3.7}$$

$$L_0 \equiv \sqrt{(X_j - X_i) + (Y_j - Y_i)}\ , \text{and} \tag{3.8}$$

$$L^* \equiv \sqrt{(x_j - x_i) + (y_j - y_i)}\ . \tag{3.9}$$

The direction cosines for the bond $\mathbf{B_j}$ in the reference configuration are defined by

$$\{n_s\} \equiv \begin{Bmatrix} \frac{(X_j - X_i)}{L_0} \\ \frac{(Y_j - Y_i)}{L_0} \end{Bmatrix}. \tag{3.10}$$

Similarly, the direction cosines for the bond $\mathbf{B_j}$ in deformed configuration are defined by

$$\{n_L\} \equiv \begin{Bmatrix} \frac{(x_j - x_i)}{L^*} \\ \frac{(y_j - y_i)}{L^*} \end{Bmatrix}. \tag{3.11}$$

Also, the components of the force state matrix $\{T\}_i$ are given by

$$\{T\}_i \equiv \frac{1}{2}\begin{Bmatrix} F_1 \\ \vdots \\ F_j \\ \vdots \\ F_6 \end{Bmatrix}_i . \tag{3.12}$$

Because two particle bonds contribute to the force, one-half is contributed by each bond.

3.4.3 SPLM Stretch and Strain

The SPLM has to correlate to classical mechanics in some manner in order to be comparable. The strain in the classical model is compared to the SPLM stretch. To do so, the strain is assumed to be very small and the stretch and the direction cosine in reference configuration given by Eq. 3.10 maps the components of strain to the SPLM stretch. It can be represented mathematically as,

$$\begin{Bmatrix} S_1 \\ \vdots \\ S_j \\ \vdots \\ S_6 \end{Bmatrix} = \begin{bmatrix} (n_{X1})^2 & (n_{Y1})^2 & (n_{X1}n_{Y1}) \\ & \vdots & \\ (n_{Xj})^2 & (n_{Yj})^2 & (n_{Xj}n_{Yj}) \\ & \vdots & \\ (n_{X6})^2 & (n_{Y6})^2 & (n_{X6}n_{Y6}) \end{bmatrix} \begin{Bmatrix} \varepsilon_{xx} \\ \varepsilon_{yy} \\ \gamma_{xy} \end{Bmatrix} \text{ or}$$

$$\{S\} = [N]\ \{\varepsilon\} \tag{3.13}$$

where n_{Xj} is the X-direction cosine of bond j. The stretch is decomposed into two components to account for plastic stretch:

$$\{S\} = \{S^e\}+\{S^p\}. \tag{3.14}$$

3.4.4 SPLM Force and Stress

In the previous section, we established the relationship between SPLM stretch and continuum strain. Similarly, we refer to the (Gerstle, 2015) three-dimension derivations, and derive the relationship between SPLM force {F} and stress {σ} of classical mechanics for plane stress and strain. For this the virtual work done by homogenous deformation in both SPLM and classical model must produce equal virtual work so that

$$\delta W_{Classical} = \delta W_{SPLM} \tag{3.15}$$

$$\delta W_{Classical} = \lfloor \sigma \rfloor \{\delta \varepsilon\} \Delta V$$

$$\delta W_{SPLM} = \lfloor F \rfloor \frac{[L_i]}{2} \{\delta S\}$$

where, $[L_i] = \begin{bmatrix} L_1 & 0 & \cdots & 0 \\ 0 & L_2 & & \vdots \\ \vdots & & \ddots & 0 \\ 0 & \ldots & 0 & L_6 \end{bmatrix}$ is a (6x6) diagonal matrix of bond lengths L_i where $[L_i]$ $= L_0 \boldsymbol{I}$ for two-dimensional case and $\boldsymbol{I}$ is the 6x6 identity matrix.

Substituting values in Eq. 3.15 we get,

$$\lfloor \sigma \rfloor \{\delta \varepsilon\} \Delta V = \lfloor F \rfloor \frac{L_0}{2} \{\delta S\}. \tag{3.16}$$

We know that $\{S\} = [N]\{\varepsilon\}$, and $\{\delta S\} = [N]\{\delta \varepsilon\}$so we get,

$$\lfloor \sigma \rfloor \{\delta \varepsilon\} \Delta V = \lfloor F \rfloor \frac{L_0}{2} [N] \{\delta \varepsilon\}, \text{ and for arbitrary } \{\delta \varepsilon\}$$

$$\lfloor \sigma \rfloor \Delta V = \lfloor F \rfloor \frac{L_0}{2} [N],$$

$$\lfloor \sigma \rfloor = \frac{L_0}{2\Delta V} \lfloor F \rfloor [N], \tag{3.17}$$

$$\{\sigma\} = \frac{L_0}{2\Delta V} [N]^T \{F\} \ . \tag{3.18}$$

Eq. 3.18 gives the relationship between the SPLM force {F} and the classical stress $\{\sigma\}$.

To simplify, $\{\sigma\} = [M]\{F\}$, and (3.19)

$$[M] = \frac{1}{2\Delta V} [N]^T L_0.$$

For planar problems, the volume ΔV of the material is given by, $\frac{\sqrt{3} t_b L^2}{2}$, where t_b is the body thickness and L is the lattice spacing. For the linear elastic model,

$$\{F\} = [K]\{S^e\}. \tag{3.20}$$

We also relate stress to strain proportionally with constitutive matrix [D].

$$\{\sigma\} = [D]\{\varepsilon^e\} \tag{3.21}$$

Multiplying both sides by [M] of Eq. 3.20 gives

$$[M]\{F\} = [M]\,[K]\{S^e\}. \tag{3.22}$$

We substitute Eq. 3.13 into Eq. 3.22 and get,

$$[M]\{F\} = [M]\,[K][N]\,\{\varepsilon^e\} \tag{3.23}$$

From Eq. 3.19, $\{\sigma\} = [M]\,[K][N]\{\varepsilon^e\}$ where, (3.24)

$[M]\,[K][N] = [D]$ and [D] is symmetric.

We now develop the stiffness matrix for the lattice topology in plane stress SPLM. So, for the six neighboring bonds in the reference configuration with length L_0, the bond force $\mathbf{F_j}$ is equal to the stretch S_j times constant 'a' plus six times the average stretch of six bonds times constant 'b'.

$$\mathbf{F_j} = aS_j + 6bS_{avg} \text{ where,} \tag{3.25}$$

$$S_{avg} = \frac{1}{6}\sum_{j=1}^{6} S_j \tag{3.26}$$

Thus, the force $\mathbf{F_j}$ in each of the six bond depends upon all bond stretches.

Now the stiffness matrix is worked out for all six bonds which is given by [K] matrix with six rows and six columns.

$$[K] = \begin{bmatrix} a+b & b & b & b & b & b \\ b & a+b & b & b & b & b \\ b & b & a+b & b & b & b \\ b & b & b & a+b & b & b \\ b & b & b & b & a+b & b \\ b & b & b & b & b & a+b \end{bmatrix} \tag{3.27}$$

In two-dimensions, [D] is given by the matrix below in terms of E and ν.

$$[D] = \frac{E}{(1-\nu^2)}\begin{bmatrix} 1 & \nu & 0 \\ \nu & 1 & 0 \\ 0 & 0 & \frac{(1-\nu)}{2} \end{bmatrix}, \text{ for plane stress and} \tag{3.28}$$

$$[D] = \frac{E}{(1+\nu)(1-2\nu)}\begin{bmatrix}(1-\nu) & \nu & 0\\ \nu & (1-\nu) & 0\\ 0 & 0 & \frac{(1-2\nu)}{2}\end{bmatrix}, \text{ for plane strain} \quad (3.29)$$

All these and other equations are derived for three-dimension in detail in (Gerstle, 2015) for [M] and [N]. Then, from [D] = [M][K][N] we solve for the values of the constants a, and b using MATLAB:

for plane stress, $$a = \frac{2ELt_b}{\sqrt{3}(1+\nu)}, \quad (3.30)$$

$$b = \frac{ELt_b(1-3\nu)}{6\sqrt{3}(1-\nu^2)}, \quad (3.31)$$

and plane strain,

$$a = \frac{2ELt_b}{\sqrt{3}(1+\nu)}, \quad (3.32)$$

$$b = \frac{ELt_b(1-4\nu)}{6\sqrt{3}(2\nu-1)(1+\nu)}. \quad (3.33)$$

We can see that the SPLM linear solution matches the classical linear solution without solving the integral equations in continuum space.

3.5 SPLM Damage Model

Damage is modelled by a reduction in bond stiffness. The model that we have used for simulation experiences both damage and plasticity, therefore, we call it an elastic-plastic model. When the force in Eq. 3.20 reaches a tensile strength value, damage is initiated, and the force is determined by $\{\mathbf{F}\} = (1-\omega)[K]\{S^e\}$ where, ω is the average damage of the two particles connected by the bond. In Fig. 3-5, referenced from (Nikravesh & Gerstle, 2018), σ_t is the tensile strength, $\gamma\sigma_t$ is the tensile damage constant at the "knee", COD_c is the critical crack opening displacement and COD_1 is the crack opening

displacement at the “knee”. In Fig. 3-6, ω increases non-linearly with respect to CODeq and reaches the maximum tensile damage parameter ω value of 1. When the damage value reaches 1, the particle is no longer associated with the material body and does not react with the neighboring particles, except when the distance between particles becomes less than the reference lattice spacing, the repulsive contact force is restored by setting ω to zero.

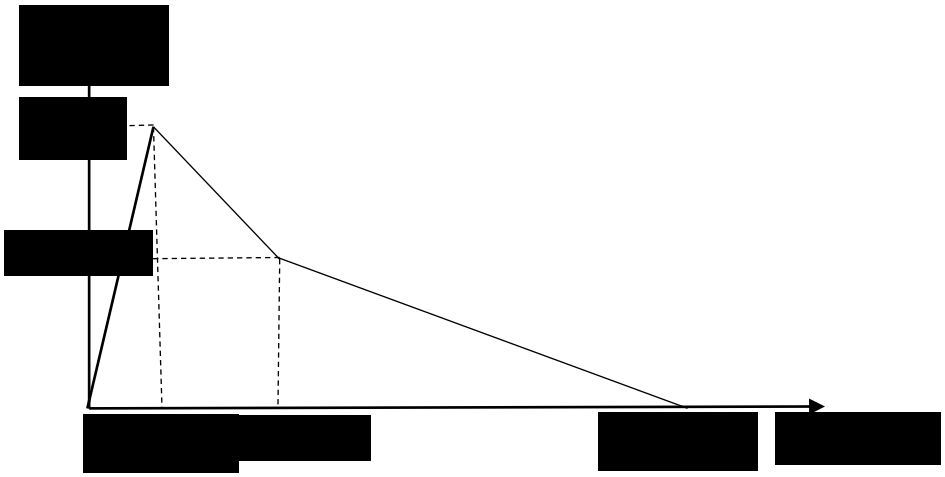

Figure 3-5 Stress versus CODeq (Nikravesh & Gerstle, 2018)

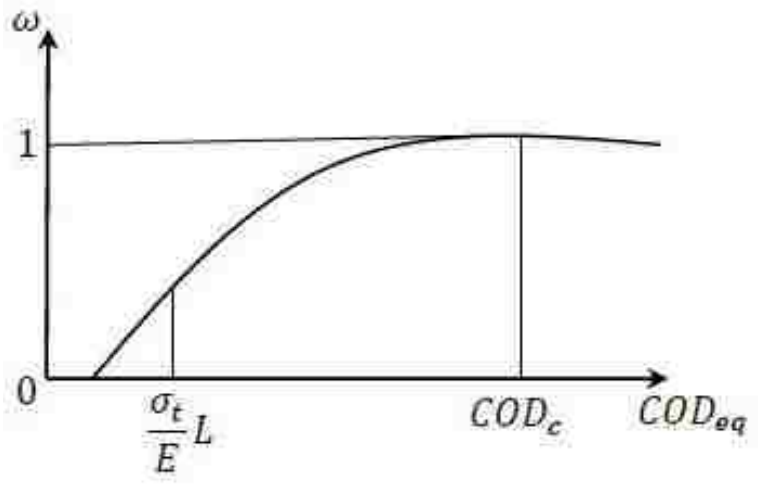

Figure 3-6 Damage versus CODeq

3.6 SPLM Plasticity Model

Using SPLM it is possible to develop an elastic-plastic model without using the classical stress-strain concept. This allows the discontinuous deformities to develop naturally and avoids the formation of stress singularities. The total stretch is assumed as the sum of elastic and plastic stretches:

$$\{S\} = \{S^e\} + \{S^p\}. \tag{3.33}$$

The bond force state is decomposed into deviatoric and hydrostatic force states:

$$\{\mathbf{F}\} = \{\mathbf{F_D}\} + \{\mathbf{F_H}\} \tag{3.34}$$

where $\{\mathbf{F_D}\}$ is the deviatoric force state matrix and $\{\mathbf{F_H}\}$ is the hydrostatic force state matrix. The particle yields when the norm of the deviatoric force state exceeds a critical value $F_{devyield}$.

Once the material yields, it develops plastic flow, which is a measure the stretch rate versus the force state, and it is given by a flow rule. This is presented in detail in (Gerstle, 2015). In the SPLM plasticity model, each of the six bonds related to the particle P_i and its neighbors is assigned a plastic stretch attribute. The attribute, called the "plastic bond stretch", is divided equally among the two particles connected through the bond. With all the known plastic stretches, the elastic stretches can be calculated as $\{S^e\} = \{S\}-\{S^p\}$ using the particle spatial position and the force matrix $\{F\}= [K] \{S^e\}$ can be thus computed.

In the next chapter, we present the laboratory experimental results, and then in Chapter 5 we present SPLM simulations of the laboratory specimens and compare the simulation results to the laboratory results.

Chapter 4 Laboratory Experiments

This chapter describes laboratory tests to determine the compressive, tensile and flexure strengths of concrete. The tests are performed to study the detailed nature of plasticity, damage, and cracking patterns developed.

Twenty-four specimens were tested from two batches of concrete. Among these, nine specimens were used for Brazilian split cylinder tests, three were used for direct tensile tests, four were used for modulus of rupture tests, and eight were used for direct compression tests. All cylinders were standard, six inches in diameter and twelve inches long. The beams for the flexure tests were three inches wide by three inches deep by twelve inches long. All these specimens were tested using a Tinius Olsen testing machine. The machine had a standard 400 kip loading frame with hydraulically operated platens that were used to apply deformations to the specimens. The main purpose of these tests is to study strengths and the patterns of crack initiation, crack propagation, and the failure mechanisms of the specimens. After casting, the specimens were treated in a wet curing room for just over a month. The cured cylinders were then tested, and the results obtained are used for comparison with SPLM analyses. The results depict the time (minutes), deformation (inches) and load (lbf) in graphical forms that were used to study the crack propagation patterns. The summarized results are presented in tabular form for each type of test. The last two numbers in the specification ID in the summary table represents the experiment number. For example, 'BR01' means the first Brazilian split cylinder test, 'DT01' is the first direct tensile test, 'FT01' is the first modulus of rupture test, and 'DC01' is the first direct compression test. Respective ASTM standards were followed for each

type of test. A displacement-controlled load of 0.05 inch/min was applied for all the experiments performed.

4.1 Brazilian Split Cylinder Test

The Brazilian split cylinder test is one of the standard methods to determine the tensile strength of concrete. Concrete develops cracks when it is subjected to tensile stresses. To determine the load at which concrete cracks, we need to calculate the tensile strength. Assuming linear elastic conditions, the peak load obtained from the laboratory test is used to calculate the splitting tensile strength f_{sp}, defined as,

$$f_{sp} = \frac{2P}{\pi * L * D} \tag{4.1}$$

where, P is the peak load carried by specimen, L is the length of the specimen, and D is the diameter of the specimen.

4.1.1 Principle of Operation

A six inch by twelve-inch-long concrete cylinder was placed between the top and bottom platen of the testing machine as shown in Fig. 4-1. A packing strip (plywood) is used between the specimen and platen to distribute the load uniformly. The strip is one inch wide and 0.125 inch thick. The load was distributed along the cylinder length by the top steel bar. Nine cylinders were tested for the splitting tensile test. The average splitting strength of the concrete was found to be 489.656 PSI with a standard deviation of 49.468 PSI and a coefficient of variation 10.103%, as shown in Table 4-1.

Figure 4-1 Laboratory set up for Brazilian splitting test

Table 4-1 Summary of test results for splitting strength

Specification ID	Batch	Specimen age while testing (Days)	Peak Load (P_{sp}), lb	Peak Load, KN	Splitting Strength (f_{sp}), PSI	Splitting Strength (MPa)
BR01	2	29	54368	241.841	480.719	3.314
BR02	1	35	60041	267.076	530.879	3.660
BR03	2	36	59490	264.625	526.007	3.627
BR04	2	37	55479	246.783	490.542	3.382
BR05	1	37	44058	195.980	389.558	2.686
BR06	2	37	55488	246.823	490.622	3.383
BR07	1	44	49734	221.228	439.745	3.032
BR08	2	45	62140	276.412	549.438	3.788
BR09	2	45	57611	256.266	509.393	3.512
Average			*55378.78*	246.337	*489.656*	3.376
Standard Deviation			*5594.669*	24.886	*49.468*	0.341
Coefficient of variation (%)			*10.10255*	*10.103*	*10.103*	*10.103*

The test cylinders are labelled BR01 through BR09. The way crack originates and propagates during the test was also documented. Details of crack origination and

propagation with their time of occurrence (Hours: Minutes: Seconds), for a typical splitting test (Test09), are shown in Fig. 4-2 from (a) through (h). The time in each figure represents the duration taken from first appearance of the crack to the final crack pattern. Plots of load versus displacement and load versus time are calculated using MATLAB and are shown in Fig. 4-3 and Fig. 4-4, respectively, for all the experiments. Red and blue circular markings in the plot represents batch one (B1) and batch two (B2) specimens respectively. The curves are shifted horizontally in all the graphs to line up the peak loads for better visual comparison of the results. Fig. 4-5 shows the bar graph representation of the peak loads for all Brazilian split cylinder tests.

4.1.2 Discussion

The rupture in all the specimens occurs through two mechanisms, namely, principal mechanism and secondary mechanism (Claudio Rocco, 1999). The principal mechanism includes the main vertical crack that originates first at the middle of the specimen, whereas the secondary mechanism includes the vertical cracks that appear on each side of principal crack near edge of the wooden strips. These secondary cracks develop after the complete expansion of principal crack from center to the boundary (Claudio Rocco, 1999). All of our experiments followed the type of cracking pattern described above. Failure of specimens are only seen after the development of secondary crack mechanisms.

Side One

(a) Side 1- time = 0.0s

Side Two

(b) Side 2- time = 0.0s

(c) Side 1- time = 7s

(d) Side 2- time = 2s

(e) Side 1- time = 10s

(f) Side 2- time = 3s

(g) Side 1- time = 17s

(h) Side 2- time = 23s

Figure 4-2 Time sequence of occurrence of crack for Test ‘BR09’

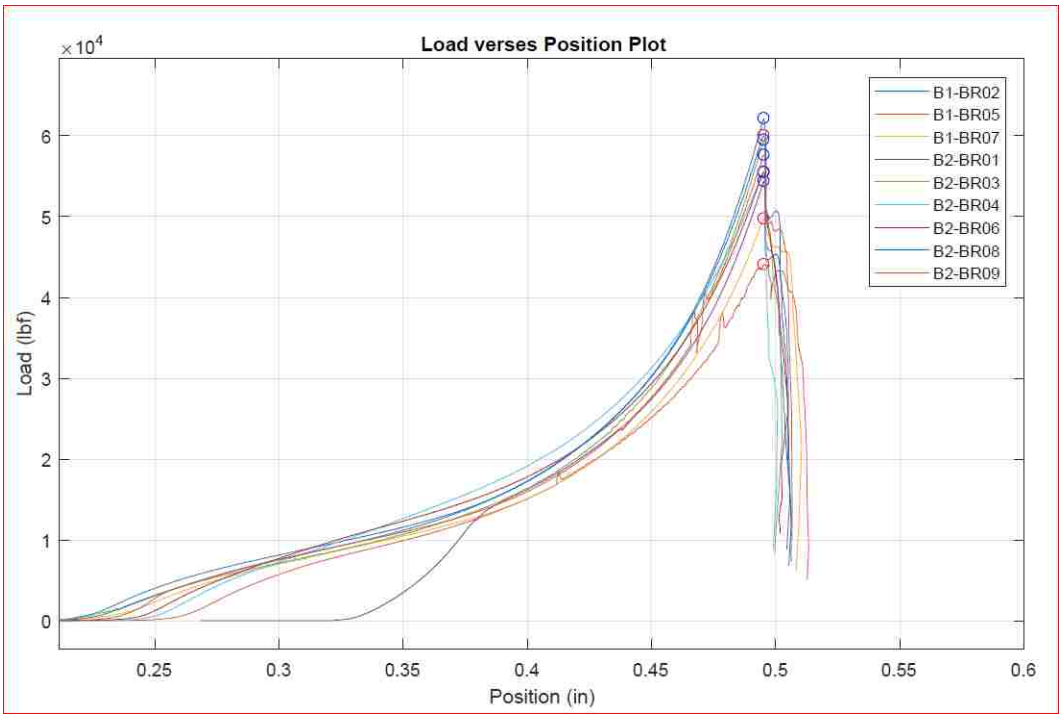

Figure 4-3 Load versus Displacement plot for Brazilian split cylinder test

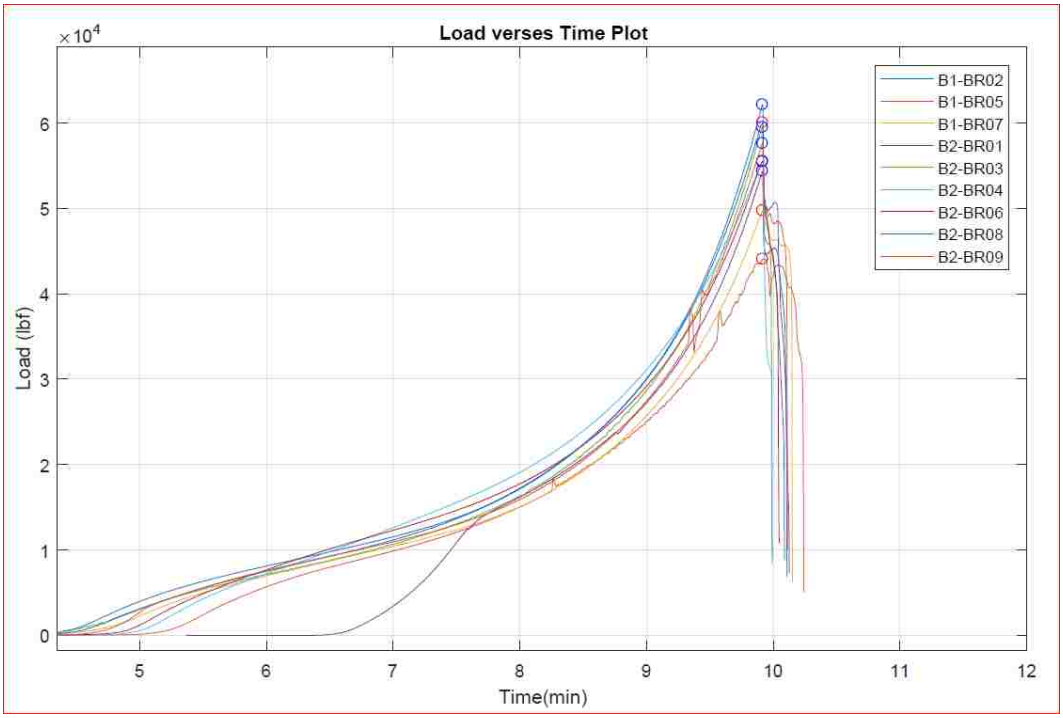

Figure 4-4 Load versus Time plot for Brazilian split cylinder test

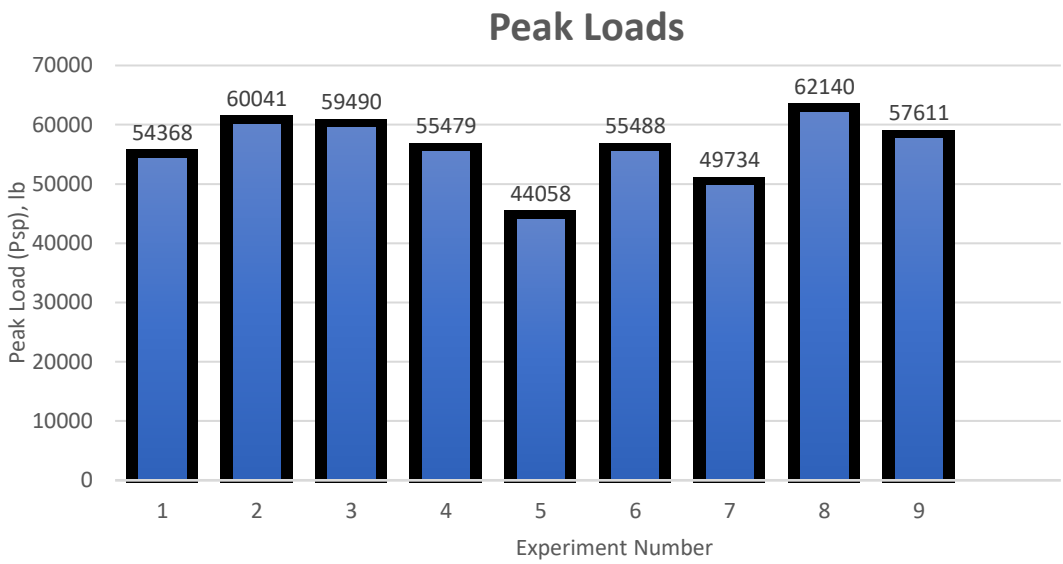

Figure 4-5 Peak loads for all Brazilian split experiments

4.2 Direct Tensile Test

The direct tensile test was nonstandard. Due to the difficulty in uniformly transferring the direct tensile load over the cross section of the specimen, embedded bolts were used to apply tensile load to the specimen as shown in Fig. 4-6. In this method, the peak load is obtained from the laboratory test and the direct tensile strength of the concrete F_t , is defined as,

$$F_t = P/A \tag{4.2}$$

where, P is the peak load carried by the specimen, and A is the cross-section area of the specimen.

4.2.1 Principle of Operation

A six inch by twelve-inch-long concrete cylinder, with a ¾" diameter bolt embedded in each end of the cylinder, was attached to the top and bottom platens of the testing machine, as shown in the Fig. 4-6. The bolts here are used to transfer the direct tensile force from the platens to the specimen. Three cylinders were tested in the direct

tensile test series. The average direct tensile strength of the concrete was found to be 275.798 PSI with a standard deviation of 12.594 PSI and coefficient of variation 4.566 percent, as shown in Table 4-2. Plots of load verses position and load verses time are calculated using MATLAB and are shown in Fig. 4-9 and Fig. 4-10, respectively for all the experiments. All these specimens are from batch one (B1 as represented in index). The final cracking pattern for different direct tensile experiments are shown in Fig. 4-7. It is noticed from these figures that the failure patterns are somewhat variable.

Table 4-2 Summary of the test results for direct tensile strength

Specification ID	Batch	Specimen age while testing (Days)	Peak Load (P_{DT}), lb	Peak Load (KN)	Direct Tensile Strength (f_{DT}) (PSI)	Direct Tensile Strength (MPa)
DT01	1	40	8137	36.195	287.788	1.984
DT02	1	42	7830	34.830	276.930	1.909
DT03	1	42	7427	33.037	262.677	1.811
Average			*7798*	34.687	*275.798*	1.902
Standard Deviation			*356.08*	1.584	*12.594*	0.087
Coefficient of Variation (%)			*4.566*	*4.566*	*4.566*	*4.566*

4.2.2 Discussion

The failure of all the direct tension tests was very sudden and dynamic. The average direct tensile strength of the concrete (7.798 5Kips) obtained from laboratory test is much lower than we expected (17 to 20 Kips). This may be due to the stress concentration near the bolt head. This specimen is considered for SPLM simulation to observe how significant the stress concentration is near the bolt head.

We calculate the concrete breakout and concrete pullout strengths based on ACI 318-14, chapter 17 (ACI Committee 318 & American Concrete Institute, 2016). It was

conducted to ensure that there will be no pulling of the bolt or breaking of the concrete chunks that would lead to different results than expected.

Strength of anchor in Tension

Gross area of bolt = 0.442 inch^2

Net area of bolt ($A_{se,N}$) = 0.334 inch^2

Yield Strength (F_y) = 36 Ksi (For A36 steel)

Ultimate Strength (F_u) = 58 Ksi (For A36 steel)

Nominal Strength of Anchor in Tension

$N_{sa} = A_{se,N} * f_{uta}$ = 22.8456 Kips (ACI 318-14, 17.4.1.2)

where, $A_{se,N}$ is the effective cross-sectional area of an anchor (bolt) in tension and f_{uta} is smaller of $1.9 * F_y$ and 125,000 psi.

Strength reduction factor (ϕ) 0.75 (ACI 318-14, R17.4.1.2)

Reduced Strength= $\phi * N_{sa}$ 17.1342 Kips

Concrete breakout strength of anchor in tension

$N_{cb} = (A_{Nc}/A_{Nco}) * \Psi_{ed,N} * \Psi_{c,N} * \Psi_{cp,N} * N_b$ (ACI 318-14, 17.4.2.1a)

$(A_{Nc}/A_{Nco}) = 1$ (For single anchor bolt)

where, $\Psi_{ed,N}, \Psi_{c,N}, \Psi_{cp,N}$ are defined in section 17.4.2.4.-17.4.2.7 of ACI 318-14

$1.5h_{ef}$ = 7.5 inch, where h_{ef} = 5 in. is the distance from centerline of the anchor to the projected failure surface.

$\Psi_{ed,N} = 1$, $\Psi_{c,N} = 1.25$ (For cast in anchors) and $\Psi_{cp,N} = 1$ (For cast in anchors)

$N_b = K_c * \lambda * \sqrt{(f_c')} * h_{ef} * 1.5$ (ACI 318-14, 17.4.2.2a)

$K_c = 24$

$\lambda = 1$ (For normal weight concrete)

N_b = 18973.666 Pounds

N_{cb} = 23717.082 Pounds = 23.717082 Kips

Φ = 0.75

Reduced breakout strength

$\phi * N_{cb}$ = 17.787812 Kips

Concrete pullout strength

$N_{pn} = \Psi_{c,p} * N_p$ (ACI 318-14, 17.4.3.1)

A_{brg}= 0.654 inch^2

$\Psi_{c,p}$ = 1.4 (For no cracking at service load)

N_p = 8*Abrg*fc' = 26160 Pounds (ACI 318-14, 17.4.3.4)

N_{pn} = 36624 Pounds = 36.624 Kips

Φ = 0.75

Reduced pullout strength

$\phi * N_{cb}$ = 27.468 Kips

Here, we can observe that the concrete break out strength in tension is 17.78 kips which is 79089 N and the pullout strength is 27.488 kips which is about 122183 N. These values are more than enough to ensure that the concrete does not break, or the bolts will not pullout of the specimen during the application of tensile load. The maximum tensile load at which the specimen experienced breaking is 34687 N for laboratory test and 44860 N for SPLM with lattice rotation of 30 degrees. Since, both the forces are less than the breakout or the pullout strengths, no such results were obtained. The comparison of the results obtained from laboratory test, theoretical analysis and the SPLM simulations are shown in Fig. 5-11.

Figure 4-6 Laboratory set up for Direct Tensile test

a) Test DT01

b) Test DT02

c) Test DT03

Figure 4-7 Observed cracking patterns for direct tensile test at the end

In fig. 4-7 a) – c), we can see that the damage takes place near the top. It is the region where the head of the top bolt is located, and the stress would be expected to be highest in this region, when considering the self-weight of the cylinder.

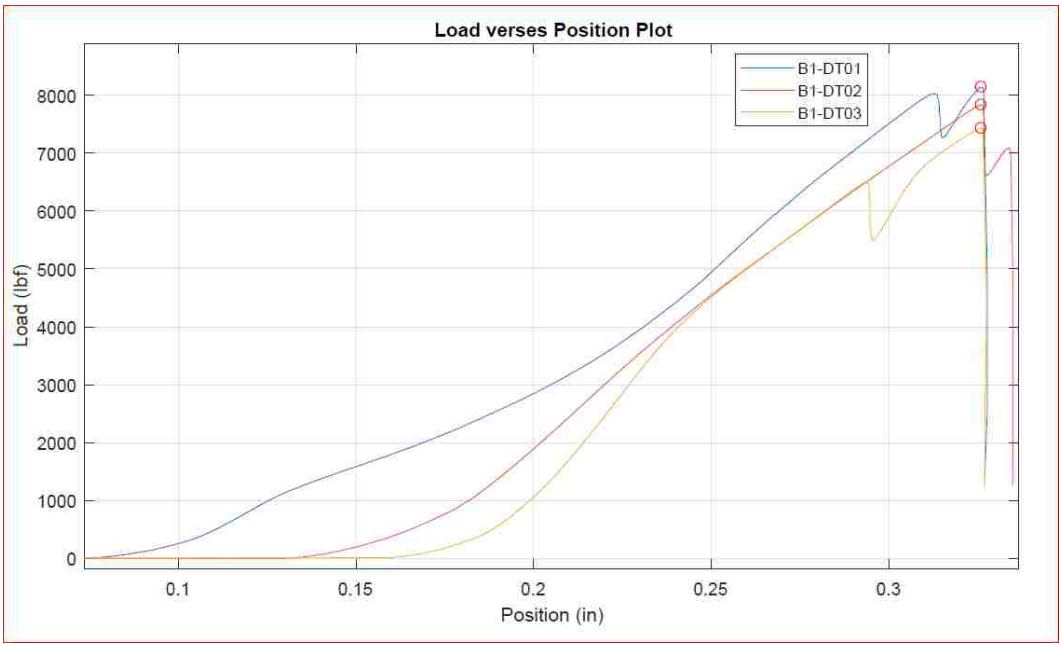

Figure 4-8 Load versus position plot for direct tensile test

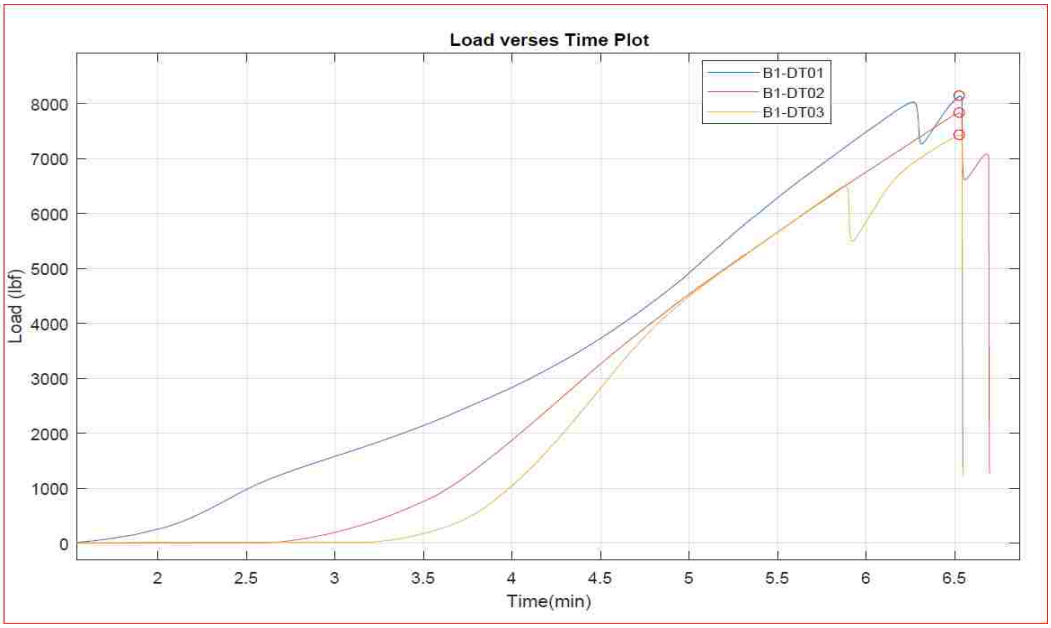

Figure 4-9 Load versus time plot for direct tensile test

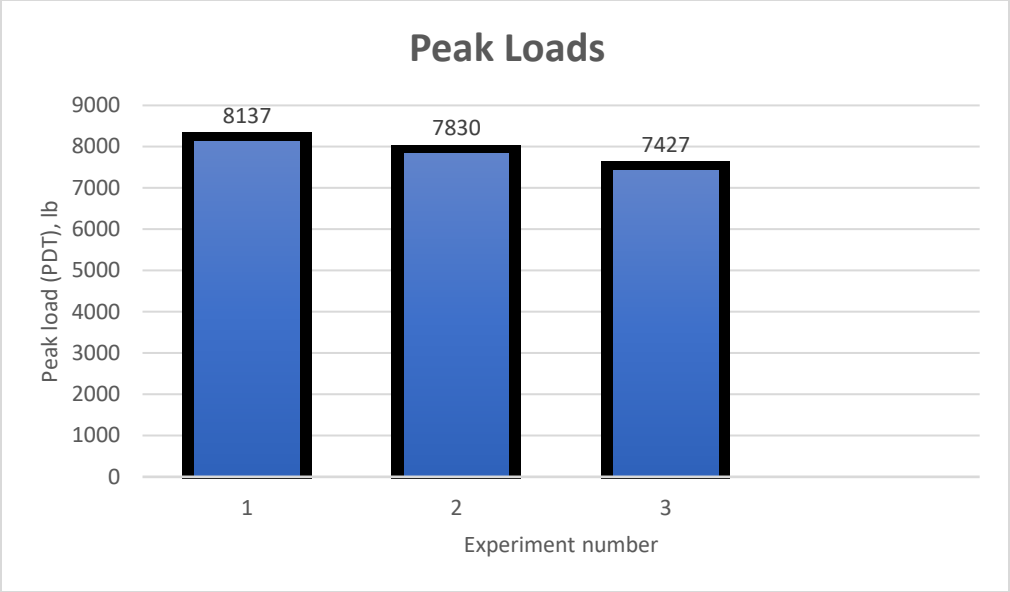

Figure 4-10 Peak loads for all direct tensile tests

4.3 Modulus of Rupture (3-point bending test)

The modulus of rupture test shown in Fig. 4-11 measures the flexural strength of the sample beams. The resulting formula for the stress under the 3-point bending test for the bar is given by:

$$\sigma_{max} = 3FL/2bd^2 \quad (4\text{-}3)$$

where F is the peak load, L is the span, b is the average width of the specimen, and d is the depth of the specimen.

4.3.1 Principle of Operation

The beam, three inches wide by three inches deep by twelve inches long, is placed centrally on two steel supports as shown in Fig. 4-11. The loading bar is set above the specimen at the center, as shown in Fig. 4-11. The beam is loaded using the hydraulic testing machine. At a certain maximum load, the beam breaks suddenly, snaps and the data are recorded using software. Four beams were tested for the modulus of rupture test. The

average modulus of rupture was found to be 838.267 PSI with the standard deviation of 45.006 PSI and coefficient of variation 5.369 percent as shown in Table 4-3.

Plots of load versus position and load versus time are calculated using MATLAB and are shown in Fig. 4-12 and Fig. 4-13 respectively for all the experiments. Red circular markings in the plot shows that all the specimens are from batch one (B1).

Table 4-3 Summary of the test results for Modulus of rupture

Specification ID	Batch	Specimen age while testing (Days)	Peak Load (lb)	Peak Load (KN)	Modulus of Rupture (PSI)	Modulus of Rupture (MPa)
FT01	1	47	**1699**	7.558	**840.886**	5.798
FT02	1	47	**1646**	7.322	**831.056**	5.730
FT03	1	48	**1846**	8.211	**895.368**	6.173
FT04	1	48	**1556**	6.921	**785.759**	5.418
Average			***1686.75***	7.503	***838.267***	5.780
Standard Deviation			***121.473***	0.540	***45.006***	0.310
Coefficient of Variation (%)			***7.20157***		***5.369***	

4.3.2 Discussion

The three-point bending test was performed to determine the modulus of rupture. Fig. 4-11 shows crack development of FT01 at two stages. Fig. 4-11 shows the cracking pattern for the laboratory experiment. Note that the crack is not centered nor vertical which means the results are somewhat indifferent. The specimens were subjected to the perpendicular load on top along the length which induced the compressive strength on the top surface and tensile strength at the bottom surface and the bar snapped into nearly two equal pieces.

Figure a: Initiation of crack; front face

Figure b: Initiation of crack; back face

Figure c: Final crack; front face

Figure d: Final crack; back face

Figure 4-11 Modulus of rupture test - Experiment 1

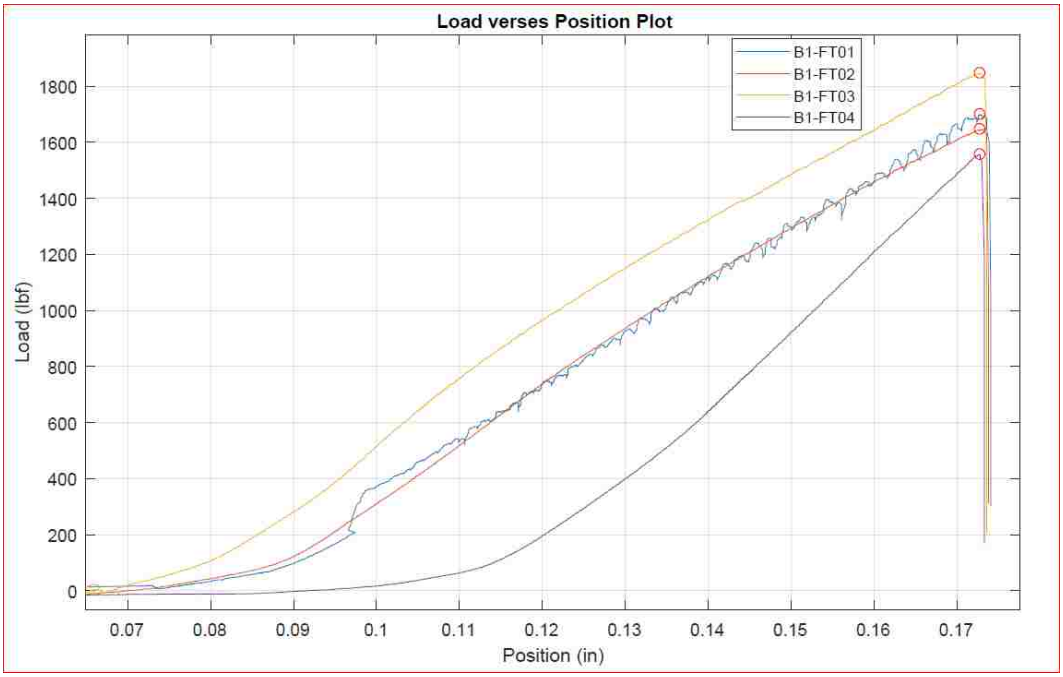

Figure 4-12 Load versus displacement plot for modulus of rupture tests

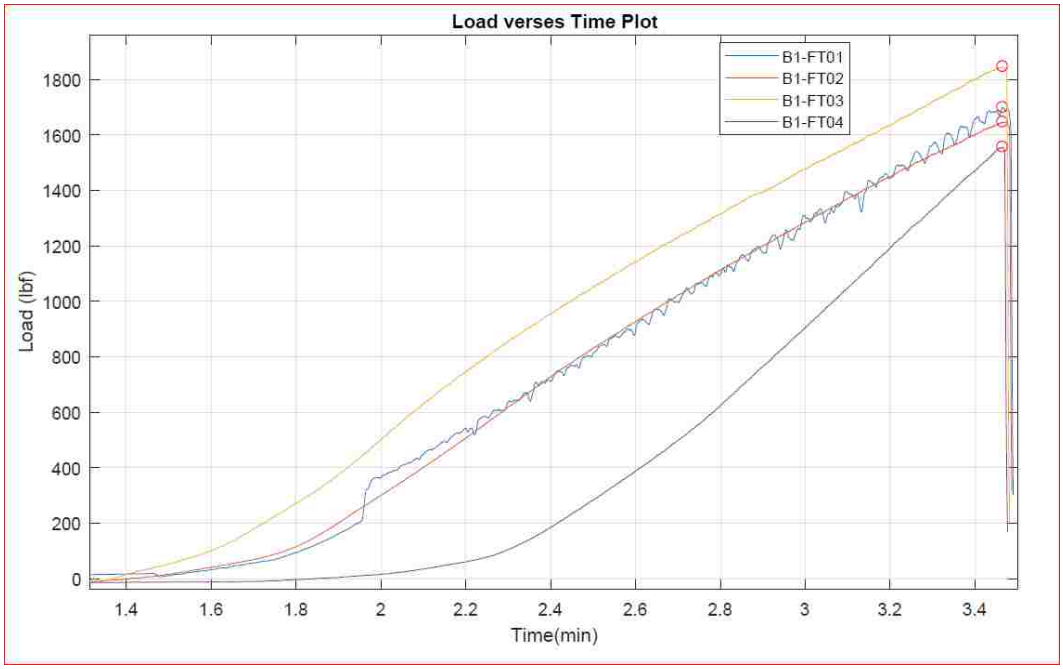

Figure 4-13 Load versus time plot for modulus of rupture tests

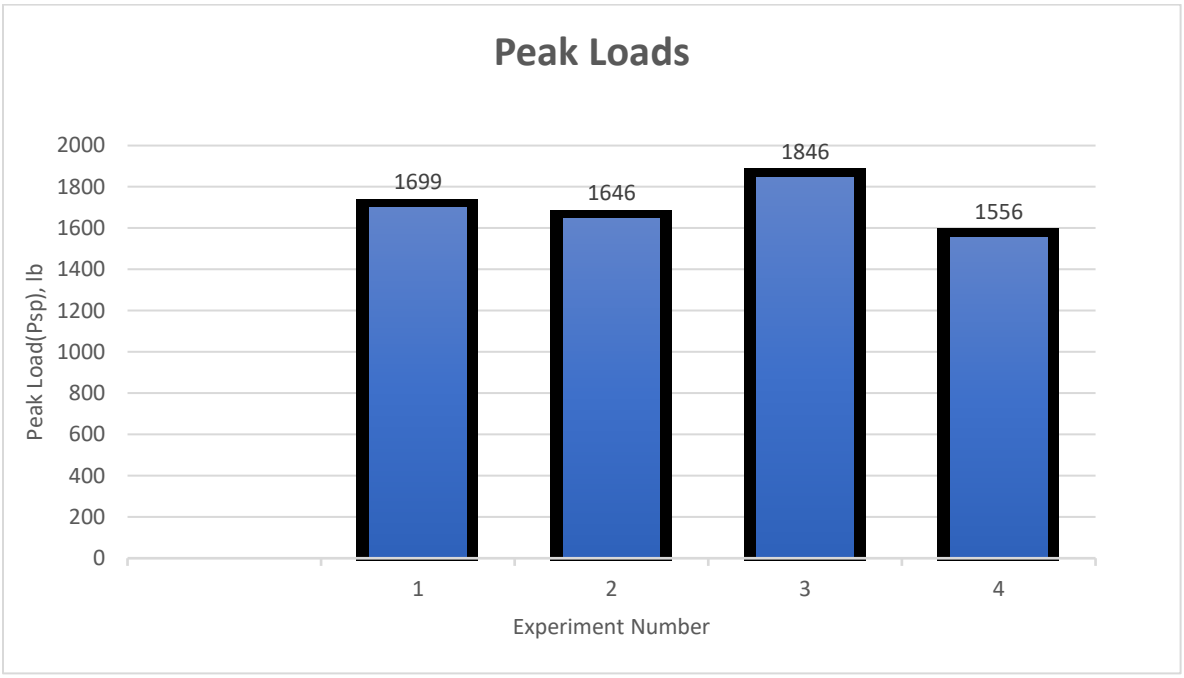

Figure 4-14 Peak loads for modulus of rupture experiments

4.4 Direct Compression Test

The direct compression test is carried out for cylindrical concrete specimens to determine both the strength and the post-strength behavior. The compressive strength is determined by dividing the peak load by the cross-sectional area.

4.4.1 Principle of Operation

The direct compression test was carried out in the same hydraulic machine that was used for the tension tests. The specimens were cylindrical and six inches in diameter by twelve inches long. They were cast in a plastic mold and cured for approximately 35-40 days. The concrete specimens were supposed to carry approximately 5000 PSI load. The specimen was placed in the machine vertically and the compressive load was applied on the top as shown in Fig. 4-15. Eight cylinders were tested for the direct compression test. Four of the specimens were tested using steel caps on top and four with the sulphur caps as shown in Fig. 4-16. For one of the cylinders in fourth experiment, a concrete vibrator was used during the casting process, for which we observed the highest value of strength (5623.481 PSI). The average direct compressive strength of the concrete was found to be 5062 PSI with the standard deviation of 421.217 PSI and coefficient of variation 8.321 percent as shown in Table 4-4. The initial and the final crack patterns for all the experiments are shown in Fig. 4-16.

The plot of load versus position and load versus time are calculated using MATLAB and are shown in Fig. 4-17 and Fig. 4-18 respectively, for all the experiments. Red and blue circular markings in the plots represent batch one (B1) and batch two (B2) specimens, respectively.

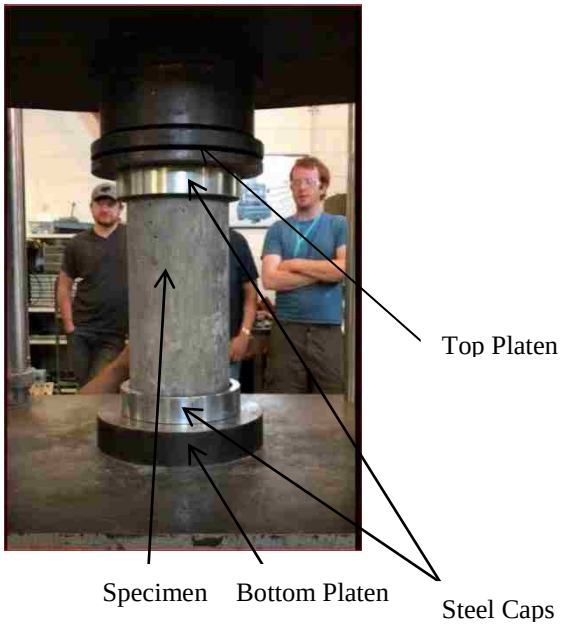

Figure 4-15 Laboratory set up for Direct Compression test

Table 4-4 Summary of the test results for direct compressive strength

Specification ID	Batch	Specimen age while testing (Days)	Peak Load (P_c), lb	Peak Load (KN)	Comp Strength (f_c') (PSI)	Comp Strength (MPa)	Remarks
DC01	2	35	127000	564.924	4491.712	30.969	Sulphur Capped
DC02	1	35	148000	658.337	5234.436	36.090	
DC03	2	36	141000	627.199	4986.861	34.383	Sulphur Capped
DC04	1	37	159000	707.267	5623.481	38.773	Vibrated
DC05	2	37	154000	685.026	5446.642	37.553	Neoprene Capped
DC06	1	37	152000	676.130	5375.907	37.066	Neoprene Capped
DC07	2	45	130000	578.269	4597.815	31.701	Sulphur Capped
DC08	1	45	134000	596.062	4739.286	32.676	Sulphur Capped
Average			*143125*	636.652	*5062.017*	34.901	
Standard Deviation			*11909.63*	52.977	*421.217*	2.904	
Coefficient of Variation (%)			*8.321139*	*8.3211388*	*8.321*	*8.321*	

4.4.2 Discussion

When the peak load occurred, the cylinder failed with a loud bursting sound. Unlike the tension tests, where the specimen failed with a single primary large crack and other secondary cracks, compressive strength test specimen failed with many cracks developing simultaneously. Sulphur caps and the neoprene caps were used to distribute the load uniformly. The neoprene caps were removable, and they produced a louder sound than the specimens with Sulphur caps. The average of the peak loads for various compressive test was 143 kips for the 5000PSI concrete.

It was observed that the sulphur-capped specimens failed at lower strength than the neoprene capped specimens. The reason might be because the neoprene cap was made from a rubber material which could store more energy. Since more energy was stored, it cracked with a loud bang. The analysis of the standard deviation of the strength of the sulphur capped and the neoprene capped specimens revealed little difference. Since both methods are ASTM approved, the results should not be altered due to the use of different capping materials.

a) Experiment-1-initial pattern

b) Experiment-1- final pattern

c) Experiment-2- initial pattern

d) Experiment-2- final pattern

Figure 4-16 Different direct compression tests performed in the laboratory

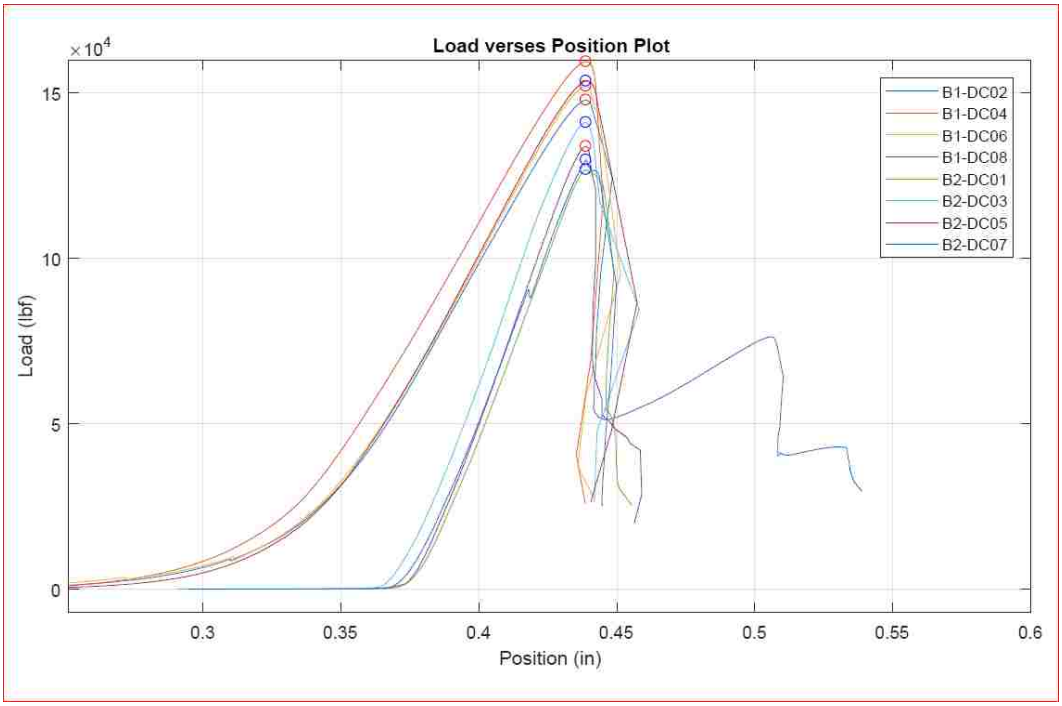

Figure 4-17 Load versus position plot for direct compression test

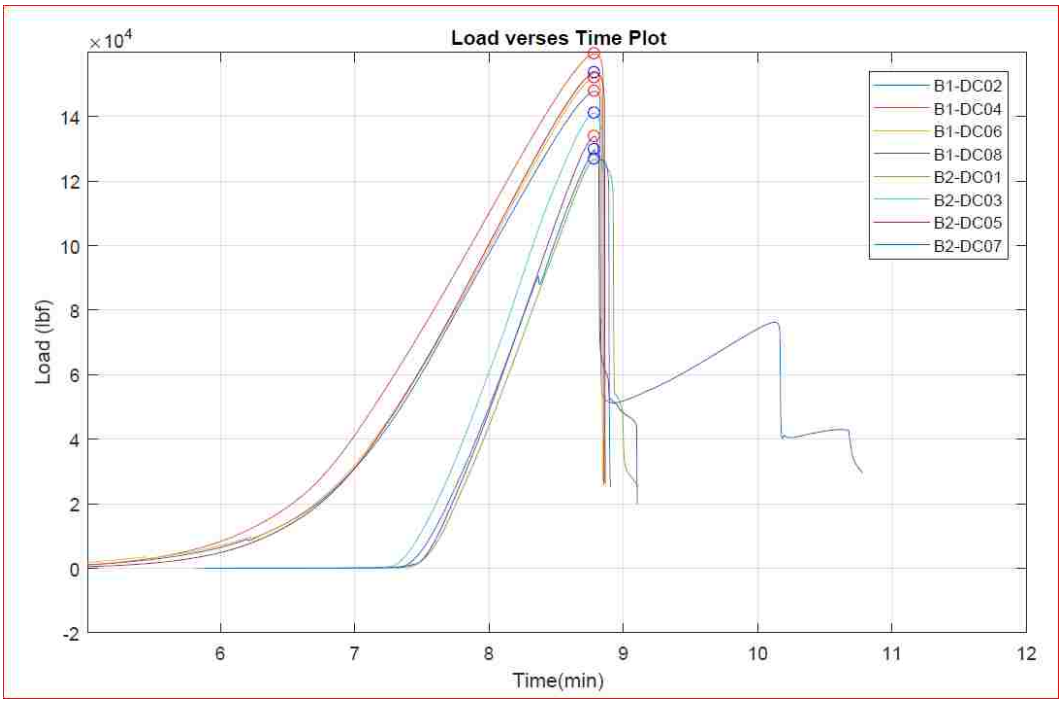

Figure 4-18 Load versus time plot for direct compression test

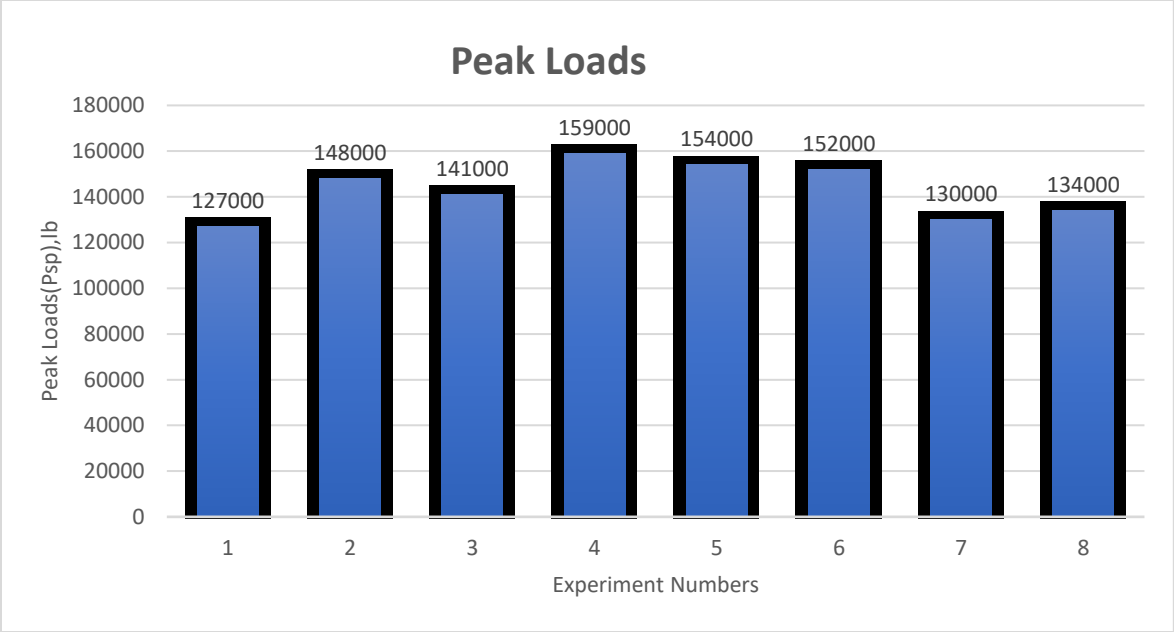

Figure 4-19 Peak load for all direct compression tests

4.5 Sieve Analysis

Sieve analysis, or the gradation test, is a procedure to determine the aggregate size distribution. The gradation of aggregate is one of the important factors that determines the strength of the concrete mix. The results from this test are often compared with standard specifications. ASTM standards ("ASTM C136 C136M 14 Standard Test Method for Sieve Analysis of Fine and Coarse Aggregates," n.d.)was mostly followed to perform the test.

4.5.1 Apparatus Used

A digital weight balance readable up to 0.1 gram was used to weigh the sample. The sieves sizes used for the test are shown in Table 4-5. The sieves used ranged from 75 micron to 4750 microns. An oven maintaining the temperature of around 110±5 degree Celsius was used to dry the sample for about 24 hours. Mechanical Sieve Shaker was used for sieving and containers and brushes were used to collect the sample.

Table 4-5 Sieve sizes used for sieve analysis

Sieve No.	200	100	50	30	16	8	4
Size (micron)	75	150	300	600	1180	2360	4750

4.5.2 Procedure

500 grams of concrete mix was taken from the ready-mix bag and washed thoroughly with water. The sample was put in the dryer for about 24 hours. Once the sample was completely dried, its weight was recorded accurately using a digital balance. The sieves of sizes shown in Table 4-5 were arranged in decreasing size from top to the bottom. The sample was placed on the top sieve and the mechanical sieve shaker was started for 10 minutes. The weights retained in each sieve were collected carefully with the help of brush and noted.

4.5.3 Results

From the sieve analysis it is observed that the grains were mostly fine aggregates as shown in Table 4-6. The rough sample weight was 500.2 grams. The weight of the sample after washing and drying was 398.7 grams. The samples were retained in each sieve and the cumulative percentage is shown in Table 4-6. The results were compared with the ASTM Standard Test Method for Sieve Analysis of Fine and Coarse Aggregates, and it was observed that the percentage passing the sieve was mostly within the range defined by ASTM.

Table 4-6 Results obtained from sieve analysis

Sieve number	Sieve size (micron)	Weight retained (gram)	Percentage of mass retained in each sieve	Cumulative percentage retained	Percentage passing
4	4750	139.1	34.892	34.891888	65.10811218
8	2360	50.7	12.718	47.609492	52.3905082
16	1180	22.24	5.579	53.18818	46.8118196
30	600	41.9	10.510	63.69839	36.30161039
50	300	70.61	17.712	81.410224	18.58977575
100	150	52.55	13.182	94.591883	5.408117193
200	75	21.26	5.333	99.924748	0.075252095
Pan	0	0.3	0.075	100	0.0
	sum	398.66			
Rough sample =			500.2	gm	
Weight of sample					
after washing and drying =			398.7	gm	
Difference in dry sample before and after sieving					0.01%< 0.3% OK

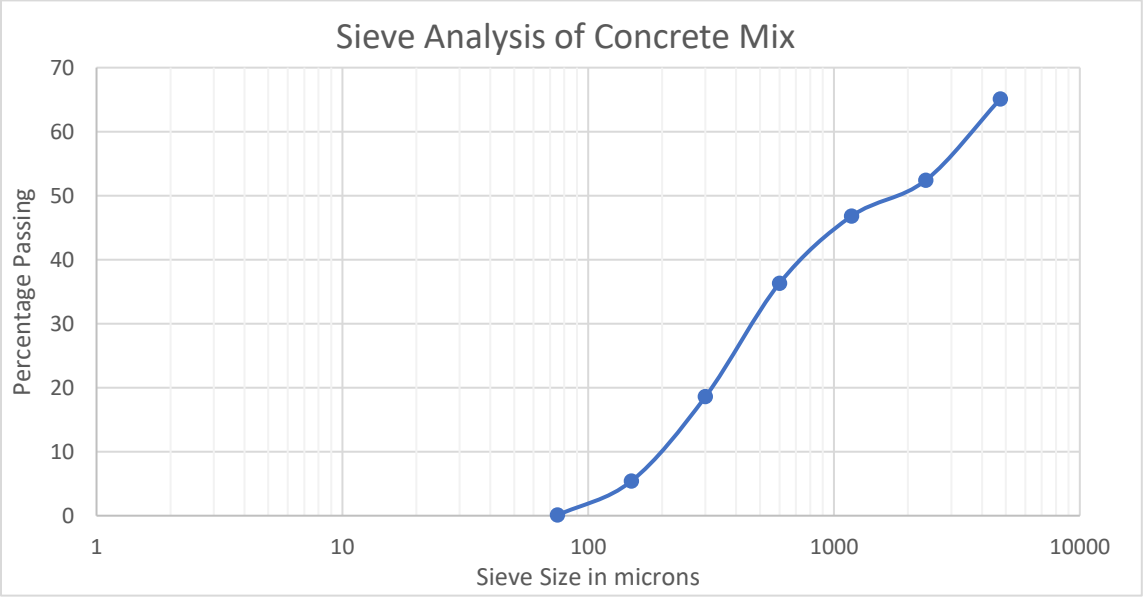

Figure 4-20 Sieve analysis of concrete mix

4.7 Conclusion

All the tests were conducted to determine not only the peak loads, but also the post-peak behavior of the cracks. The laboratory experiments were conducted under the normal conditions and the cracks obtained in the splitting, compression and tension specimens were analyzed using the SPLM software, presented in Chapter 5 in this thesis. The post-peak load analysis using the peridynamic models are studied to validate the SPLM.

Chapter 5 SPLM Validation

In this chapter, we validate the SPLM elasticity, plasticity and damage models for plain concrete. The SPLM results are compared with the laboratory results and ACI code.

5.1 Computational Implementation

The numerical simulation can be performed either in a single processor computer or a multi-processor computer. In a multi-processor computer, parallel processing can be done through MPI (Message Passing Interface). Using the multi-processor reduces the time taken to simulate the specimen. In SPLM, a single processor can simulate the specimen with maximum of 5000 particles. For specimen with number of particles more than 5000, parallel processor is required. In the parallel processor, particles will be arranged in an array of cells of size slightly greater than the horizon. Each particle will only be interacting with the particles in the own cell and direct adjacent cell. We assign eighteen particles to a 3D cell and 27 cells to a 3D array. The number of force interactions without the arrangement is $\frac{{N_p}^2}{2}$, where N_p is the number of particles. After the arrangement it reduces to $\frac{N_p * N_A * N_Q}{2}$ where, N_Q is the number of particles per cell which is 18, N_A is the number of adjacent cells in an array which is 27. So, if the number of particle is 1 million, $\frac{{N_p}^2}{2} = 5 * 10^{11}$ and $\frac{N_p * N_A * N_Q}{2} = 242 * 10^6$ which is less than without the cell decomposition (Gerstle, 2015). This significantly reduces the number of time step of calculation and also reduces the total time taken for the simulation.

For this thesis, the requirement of parallel processor was fulfilled by Center for Advanced Research Computing (CARC). The existing Fortran code is used to run the simulation and the results are displayed using MATLAB. Two programs, *Cmder* and

WinSCP are used to run the program remotely at CARC. *Cmder* provides a prompt window to give commands to CARC remote computer and *WinSCP* is used to transfer files from remote computer to the local computer. The simulation produces numerous output files that can be opened using notepad. The SPLM files are UserInput, link files, histSet files, particle post processing files, output, stress and strain files. The FORTRAN files that the user might alter are userModel.F, userIntegrate.F and userVariables.F. And finally, there is a *writeout* file that writes the output to the SPLM files.

5.2 Brazilian Split Cylinder using SPLM

Brazilian split cylinder test is an indirect tensile test which is performed to measure the tensile strength of concrete. In 1943, Lobo Carneiro and Barcellos proposed this test at the Brazilian Association for Standardization Conference. The concrete cylinder is subjected to a diametrical compressive load which results in transverse tension at the middle of the specimen (Wosatko, Winnicki, & Pamin, 2011). The tension is perpendicular to the direction of force applied and causes splitting of cylinder. Secondary and tertiary cracks are also formed due to the applied force and its reaction. This result can be seen in Fig. 5-1 a) & b) below, obtained from laboratory testing.

Figure 5-1 a) Front view of the Brazilian split cylinder b) Close up view of a cylinder

The specimen size is the same as used in the laboratory experiment. We define a number of parameters and attributes before modelling the specimen as shown in Table 5-1.

Table 5-1 Material parameter used for concrete in SPLM simulation

Parameter	English Value	SI Value
Compressive Strength, F'_c	5000 PSI	34.47379 MPa
Young's Modulus, E	4075.56 KSI	28.1 GPa
Mass density, ρ	145 PSI	2323 kg/m^3
Poisson's ratio, ν	0.2	0.2
Tensile damage parameter γ	0.25	0.25
Damping ratio, internal	0.2	0.2
Damping ratio, external	0.2	0.2
Tensile strength of concrete	353.55 PSI	2.4375 MPa
Damage initiating strain	0.003	0.003

The diameter of the model is 6 inches and the thickness is 12 inches. We assume a plane stress disk of thickness equal to the length of the cylinder. The boundary conditions are such that we apply displacements as shown in Fig. 5-2.

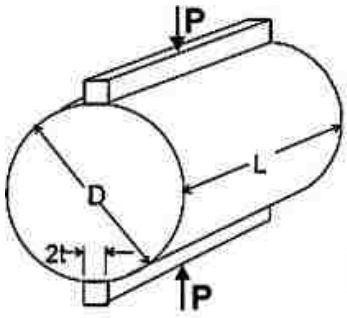

Figure 5-2 Brazilian split cylinder under compressive loading

Source: https://www.sciencedirect.com/science/article/pii/S2214509515300061

The lattice spacing used is 0.005m. The applied force generates the stresses which is then distributed along the diameter of the specimen. The linear elastic stress distribution along the diameter is shown in Fig. 5-3.

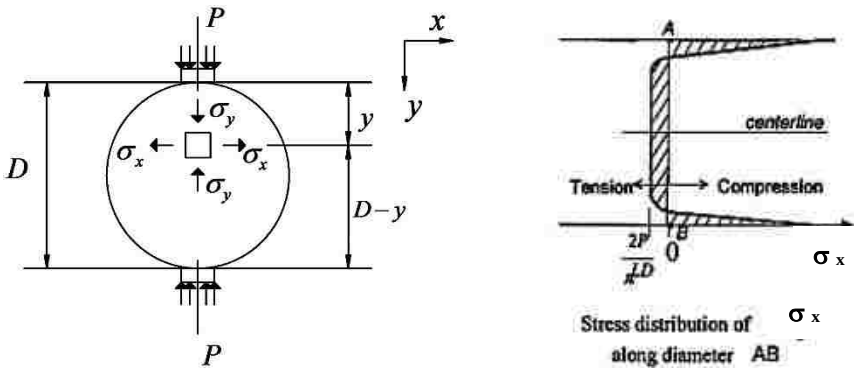

Figure 5-3 Stress distribution along the diameter

Source: https://www.sciencedirect.com/science/article/pii/S2214509515300061

A time-varying displacement $\Delta(t) = (\frac{\Delta max}{2})(1 - cos(\frac{\pi t}{t_{ramp}(end)})$ (Gerstle, 2015) is applied to the specimen at the top and bottom boundary. In the above equation, Δ_{max}= -0.0001 and t_{ramp}(end)=0.8*end time and end time is calculated based on lattice spacing, damping factor and fundamental period of vibration. The force-displacement curve obtained from the SPLM simulation for the splitting tensile test is shown in Fig. 5-4.

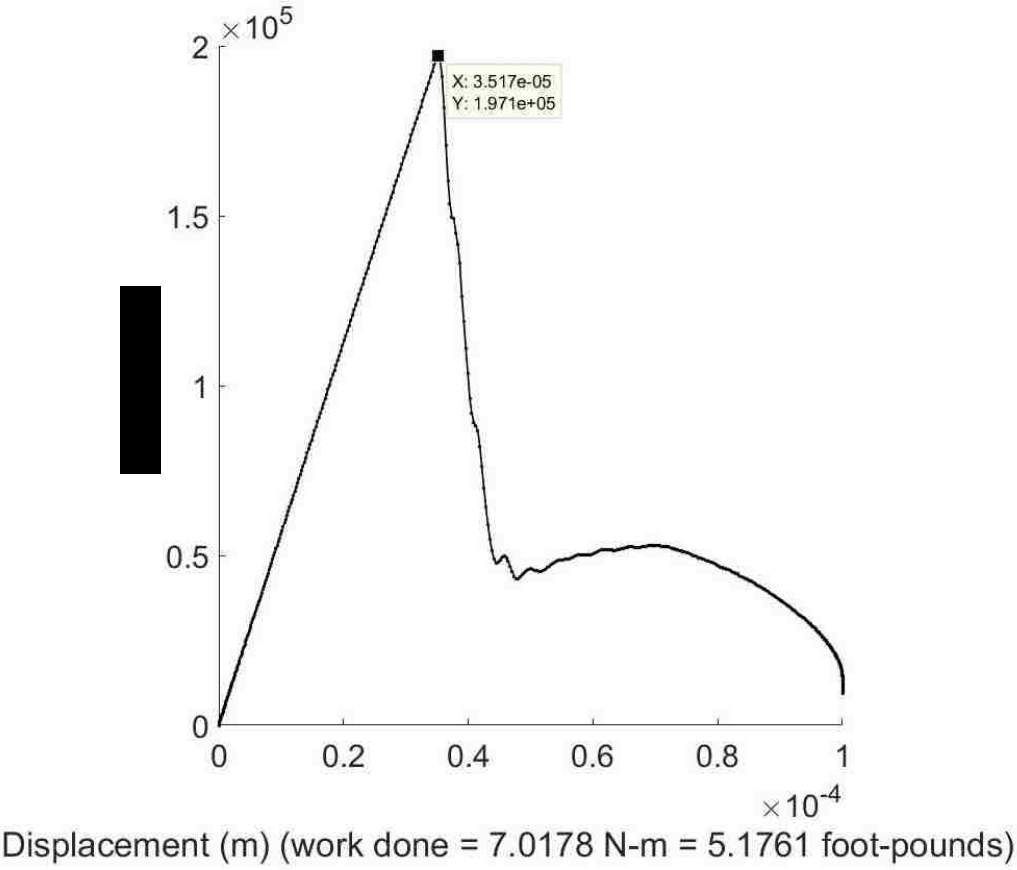

Figure 5-4 Force-Displacement relation of Brazilian Split cylinder for 0-degree lattice rotation

The graph in Fig. 5-4 demonstrates the peak load at which the cylinder fails and the displacement during that peak load. The peak load is 1.971*10^5 N for zero-degree lattice rotation. In Fig. 5-5, Fig. a, b, and c are rotated through 0°, 15°, 30° counterclockwise with the number of particles 839, 841 and 843 respectively. The number of time steps which is 6000, remains the same despite the rotation.

In Fig. 5-5, the particles in the black are yielded particles i.e. particles undergoing plastic deformation and the particles in the red are completely damaged particles. The particles can yield even if they do not get damaged. For the SPLM simulation, the displacement is applied to the particles that fall within the length which represents the width of the loading strip used in the laboratory experiment to obtain more accurate results.

The effect of the loading strip incurred is accommodated in the theoretical result by introducing β in the equation of peak-load given by,

$$P_n = \frac{(\pi l D f_{ct})}{2(1-\beta^2)^{1.5}}$$ (Nikravesh & Gerstle, 2018) (5.1)

where, l is length of the specimen, D is the diameter of the specimen, β=loading strip width/diameter, f_{ct} is the splitting tensile strength and P_n is the peak load.

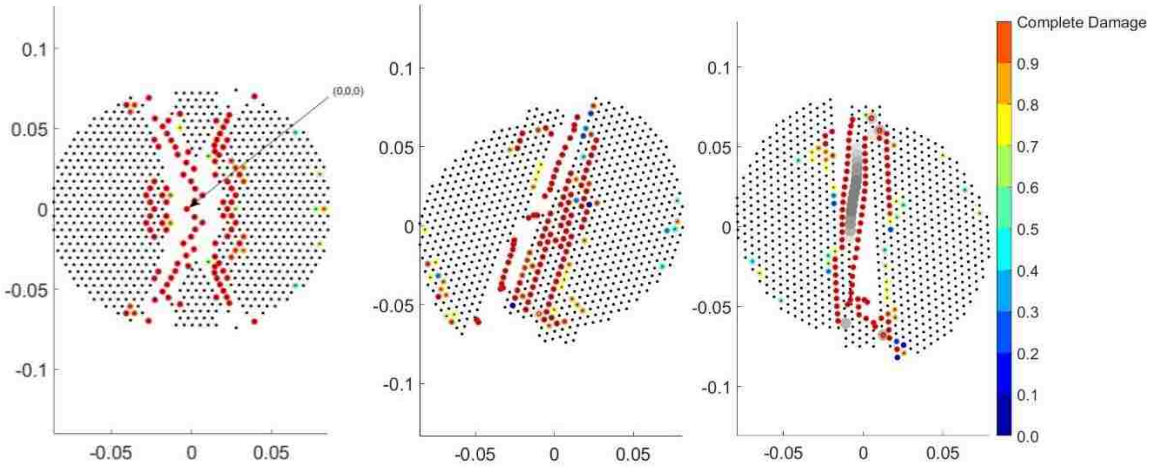

Figure 5-5 Cracking patterns obtained for Brazilian Splitting test specimen whose particle lattice is rotated through a)0, b)15 and c)30 degrees

The theoretical peak load from Eq. 5.1 is 7.33 percent low than the 0° rotated lattice and 1.22 percent low than the 15° rotated lattice and it is 2.83 percent higher than the 30° rotated lattice. The crack pattern differs in the physical appearance for different lattice rotation however, the yield stress does not vary much.

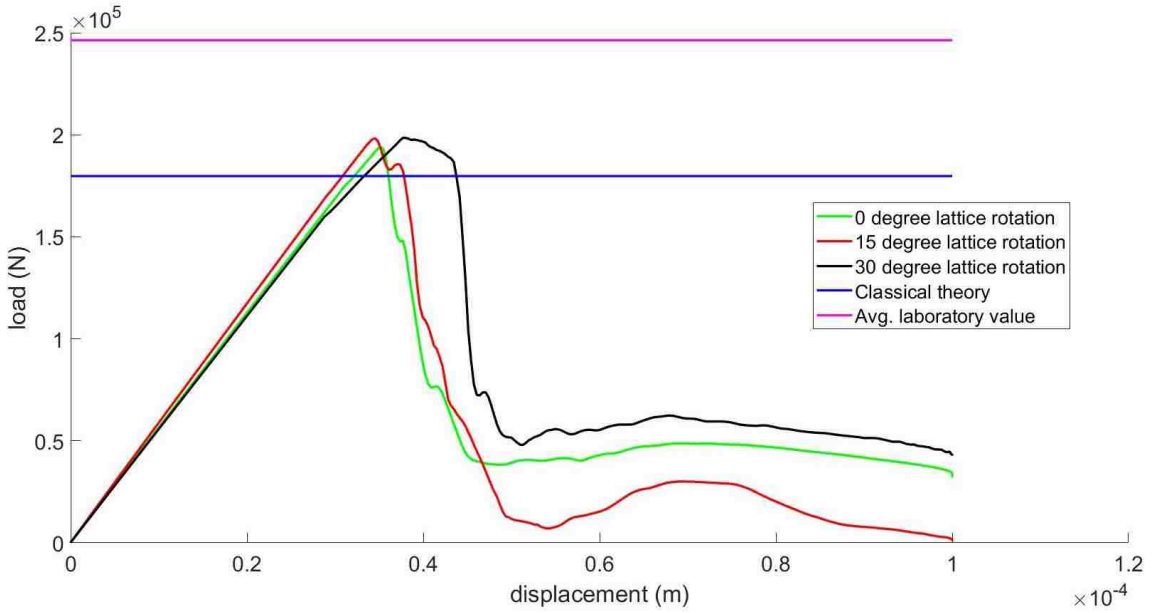

Figure 5-6 Load comparison between different SPLM lattice rotations, laboratory value and classical theoretical value for the Brazilian splitting test.

The load versus displacement graphs are plotted in Fig. 5.6. We observe that the load values obtained from SPLM for 0 and 15-degree rotation lies between the theoretical value and the average laboratory values. It is assumed that the cylinder follows the classical linear elastic theory until the peak load where it cracks along the diameter. When the vertical crack occurs, the cylinder is no longer linear elastic and demonstrates non-linear behavior. The irregularities that occur after the peak load are caused by the dynamic behavior of the particles. The potential energy is released in the form of dynamic energy which ultimately dies out due to damping. Fig. 5-7 shows the relationship between displacement and time, load and time and load and displacement respectively for the set of particles defined as boundary on the top loaded region.

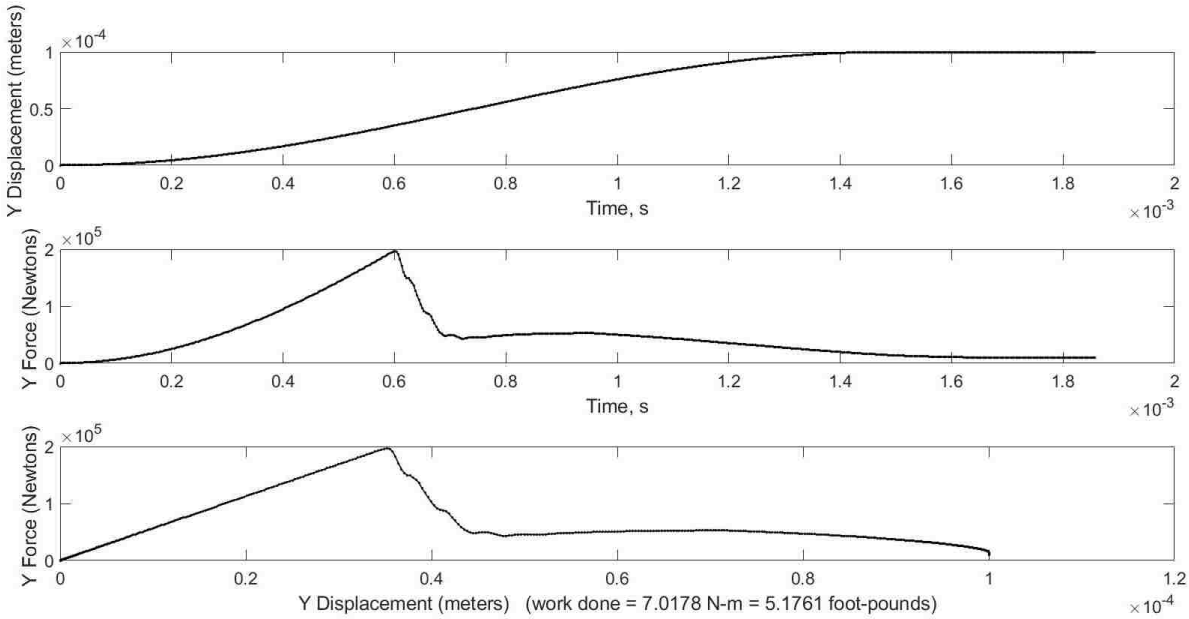

Figure 5-7 Plot of a) displacement vs time b) force vs time c) load vs displacement of particles at top loaded region of Brazilian split specimen

5.3 Direct Tension Test using SPLM

For the direct tensile test, we use the cylinder 0.3 m high by 0.15 m wide. The cylinder is then subjected to the uniaxial tension force. The force is applied as the time varying displacement at the upper boundary perpendicular to the diametric plane. The boundary condition is defined such that the load is defined along them to represent the pulling force applied as a displacement parameter. The lattice spacing of the particles used is L = 0.01m. The simulation model is as shown in Fig. 5-8.

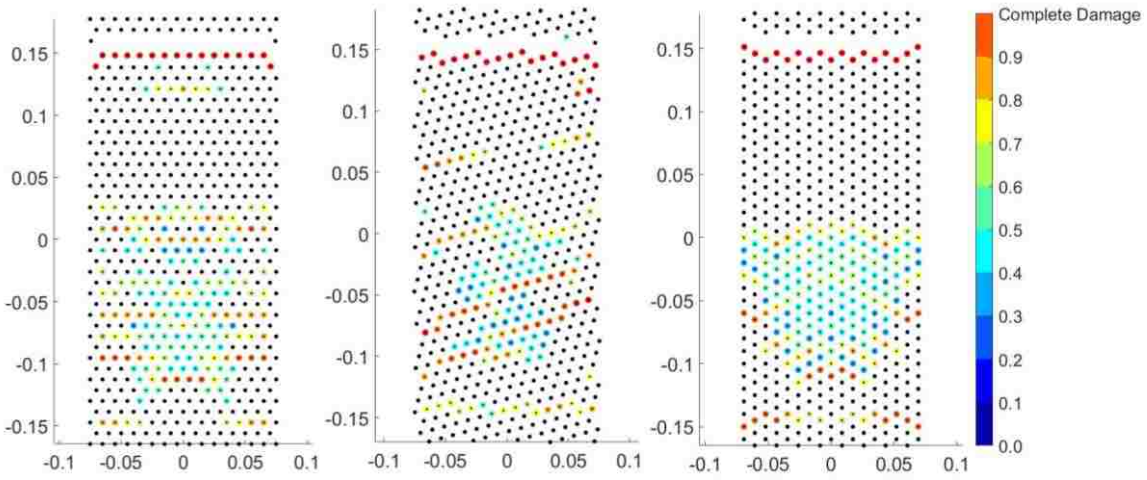

Figure 5-8 Cracking patterns obtained for direct tensile test specimen whose particle lattice is rotated through a)0, b)15 and c)30 degrees

It is normally not possible to apply tensile force to the cylinder without any prop. Hence, a bolt with a hexagonal bolt head have been embedded in the cylinder so that the tensile force can be easily applied. The boundary condition is applied such that the lower boundary is fixed and the tension (pulling) force is applied to the bolt in the upper boundary. We fixed the lower boundary assuming that it will resist the force equal to the force applied in the bolt causing the effect as if the cylinder was being pulled from both the ends. The damage and the plasticity are shown in Fig. 5-9. It is observed that the breaking of the cylinder takes place at the region of bolt-head location. In Fig. 5-9, we can see that the breakage is aligned along the lattice planes. This test, however, cannot be categorized as a pure tension test. The stress and the strain field around the region is complicated because there is a local stress concentration in the bolt head region which causes the breakage in the region where the steel particles of the bolt head interact with the concrete particles of the cylinder. The stress and the strain relationship of the particle at the center for 0-degree lattice rotation is shown in Fig. 5-10. The unusual graph in Fig. 5-10 c) is observed because of the stress concentration at the bolt head region.

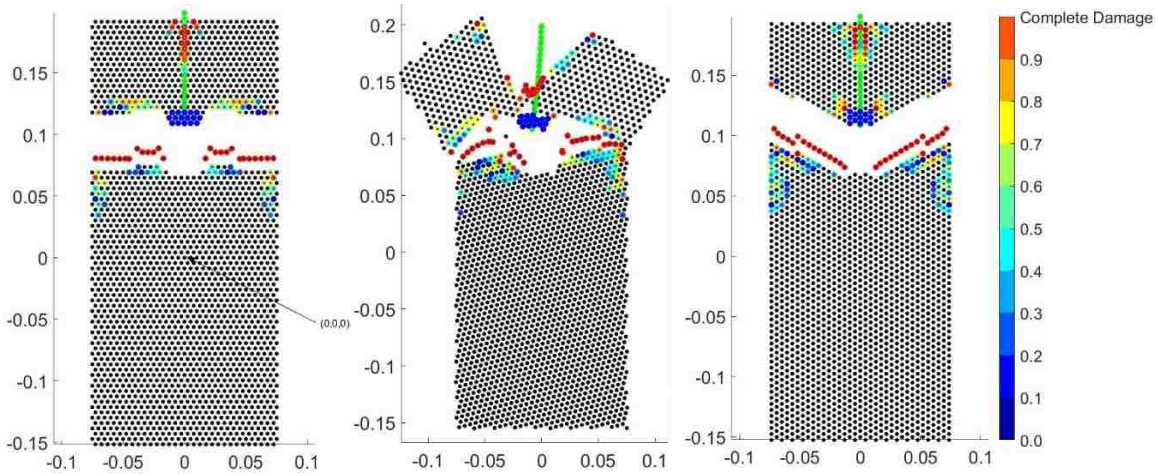

Figure 5-9 Cracking patterns obtained for direct tensile test with embedded bolts whose particle lattice is rotated through a) 0, b) 15 and c) 30 degrees

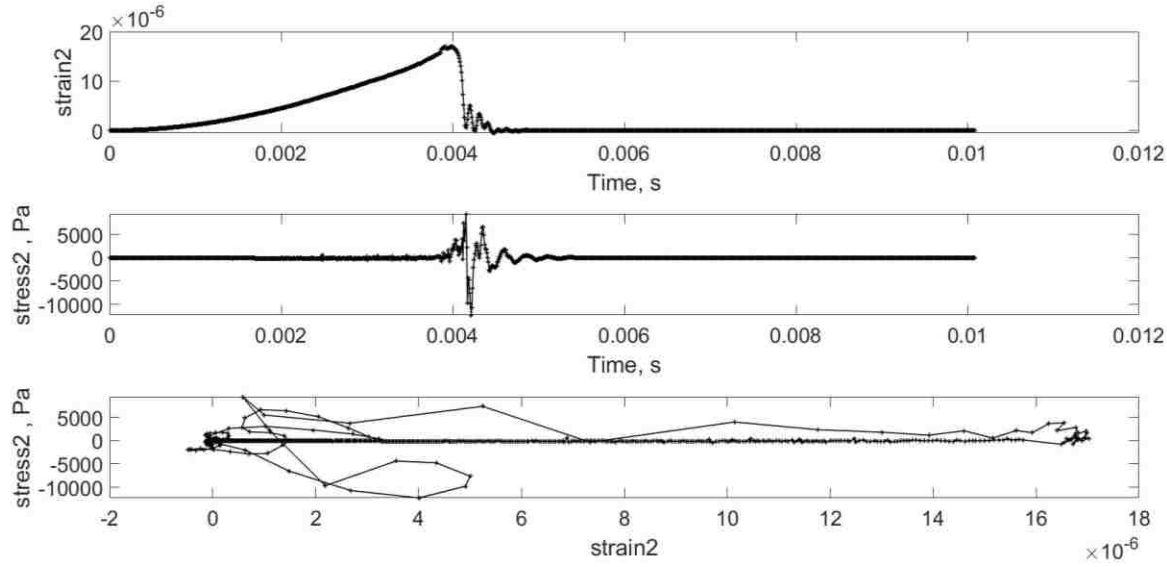

Figure 5-10 Plot of a) strain vs time b) stress vs time and c) stress vs strain of particle near the bolt head shown in figure 5-9

This SPLM direct tensile simulation is compared with the direct tensile experiment using the anchored bolts in laboratory. The SPLM simulation is performed with the cuboid of the same width and depth instead of the cylinder for 2-dimensional analysis. The loads obtained from theoretical calculation and laboratory results are for the cylinder. Therefore, these results are multiplied by the ratio of cross-sectional area of cuboid to cylinder and

obtain the loads for cuboid. The loads obtained from both is then compared with SPLM simulations as shown in the Fig. 5-11.

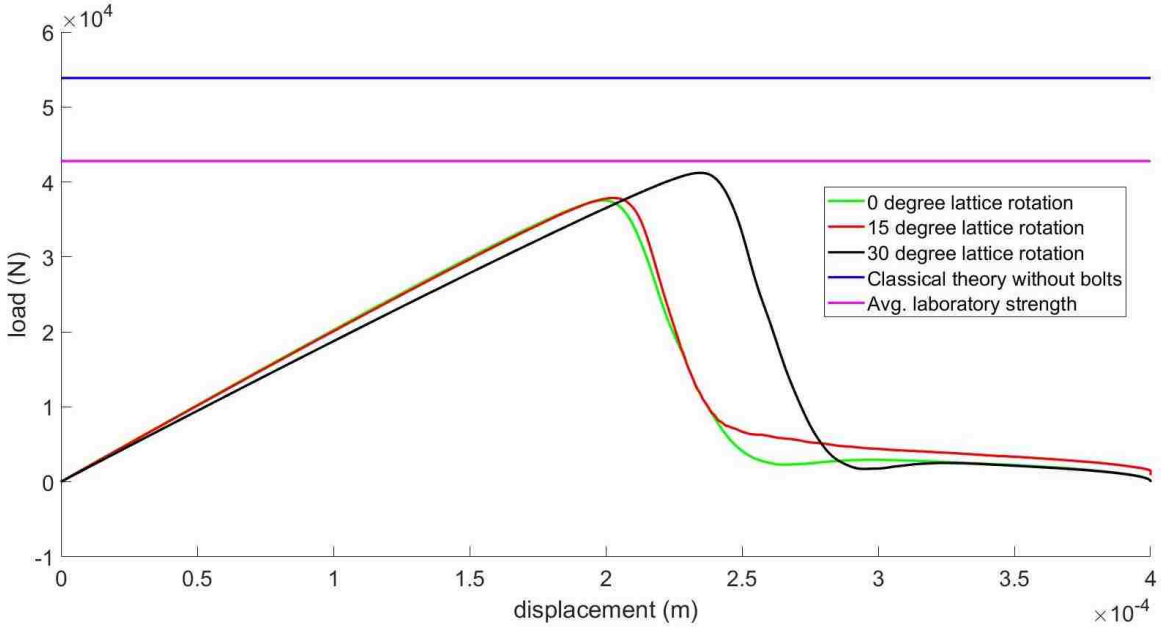

Figure 5-11 Load comparison between different lattice rotations, laboratory value and theoretical value for direct tension test

The bolt is then shifted to the side by 1/4th distance. Now it is located at 1/4th distance from the left as shown in Fig. 5-12 and 3/4th from the right side of the specimen. It is observed that the shift in the bolt causes the cylinder to break at lower peak load than when the bolt is at the center. For the bolt at 1/4th location from the left and with lattice rotation 0 degree, the peak load required to break the cylinder is 20570 N. For the same location of bolt with lattice rotation 15 degree, the peak load is 18460 N and for 30-degree location is 21130 N. We observe that the cracking pattern obtained is almost like when the bolt was at the center. The cracking is first observed at the edge near the bolt. It may be because the stress is more near the bolt and it progresses first to the nearest edge and slowly to the opposite edge. The stress concentration is felt at the zone where the bolt head is located shown in Fig. 5-12.

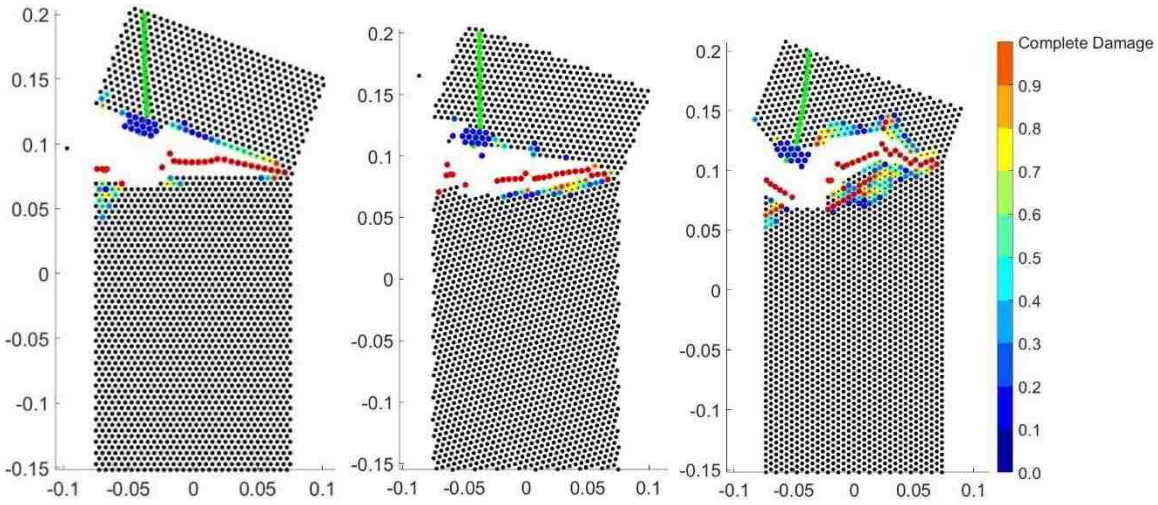

Figure 5-12 Cracking patterns obtained for direct tensile test with bolts at 1/4th length from left and whose particle lattice is rotated through a) 0, b)15 and c)30 degrees

5.4 Modulus of Rupture using SPLM

Modulus of Rupture also known as flexural strength or bending strength is the measure of transverse strength of concrete. For this test, a plain concrete beam of dimension 3 inches wide by 3 inches thick by 12 inches long is designed similarly as other tension specimen. It is then subjected to the one-point bending load in the middle of the specimen in the direction perpendicular to the cross-section of the specimen. The results obtained is shown in Fig. 5-13 and Fig. 5-14. We can see that the cracking force is 8626 N. In the load comparison figure shown in Fig. 5-16, it is noticed that the classical theory strength is significantly lower than the SPLM and the laboratory strengths. It is because the classical theory assumes that the specimen can take no more load after the initial crack is formed while with the simulation and laboratory tests we can see that it can take more load even after the initial crack is formed.

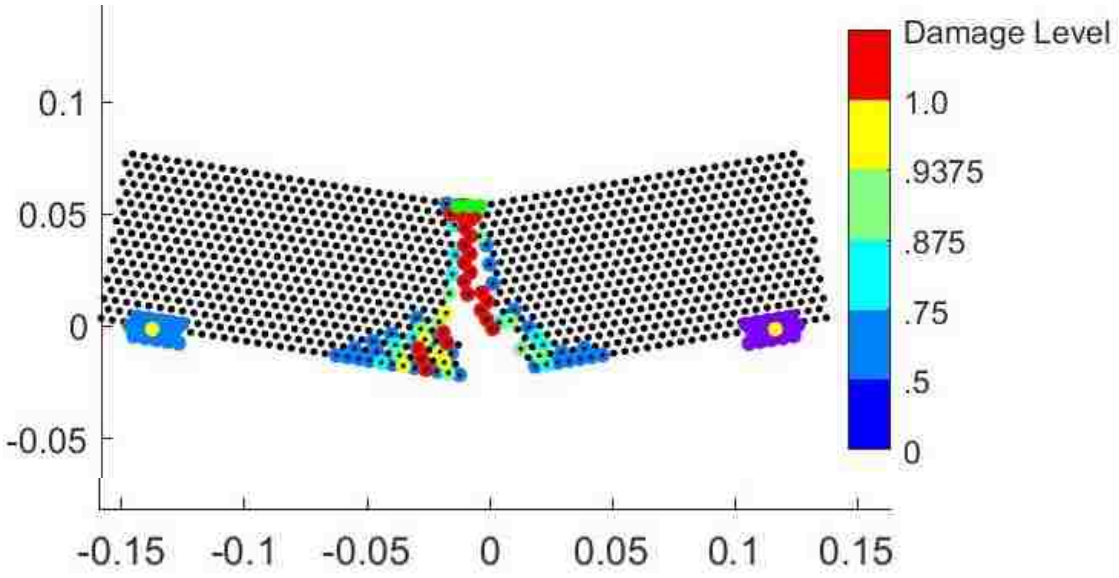

Figure 5-13 Modulus of rupture experiment using SPLM

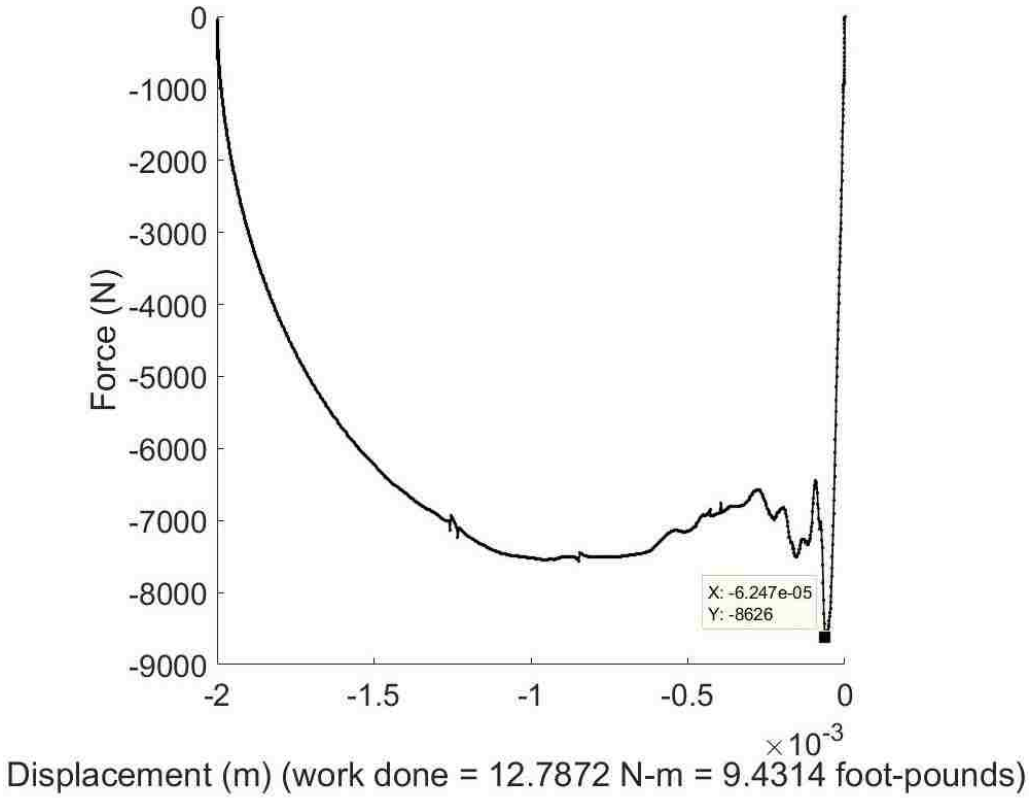

Figure 5-14 Load versus displacement graph for modulus of rupture test for 0-degree lattice rotation

The relationship of displacement with time, load with time and load with displacement is shown in Fig. 5-15 and the load comparison is shown in Fig. 5-16.

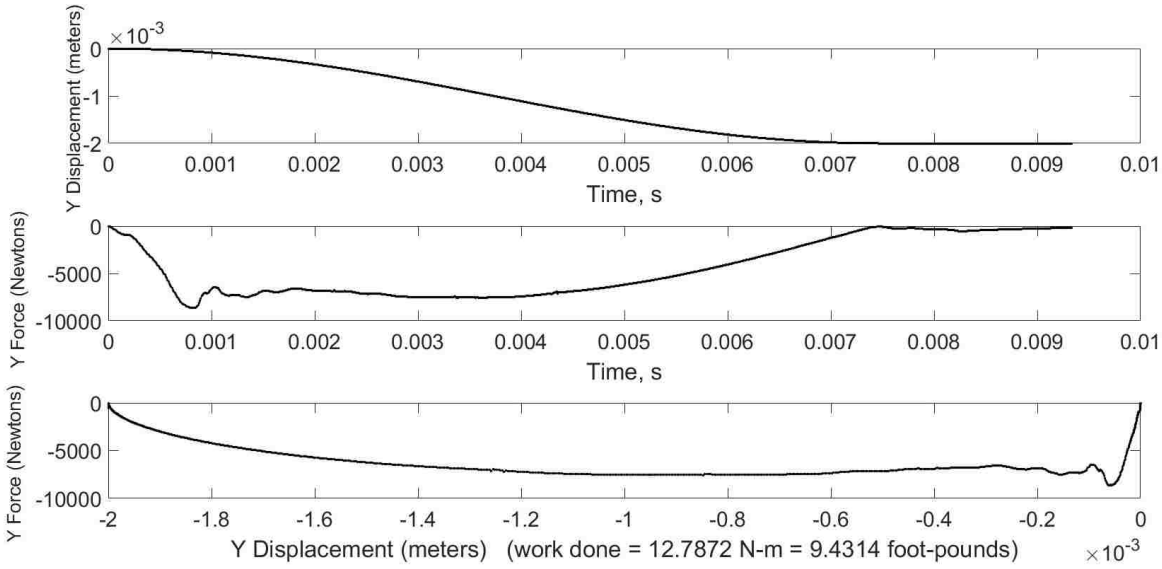

Figure 5-15 Plot of a) displacement vs time b) force vs time c) load vs displacement of particles at top loaded region of modulus of rupture specimen

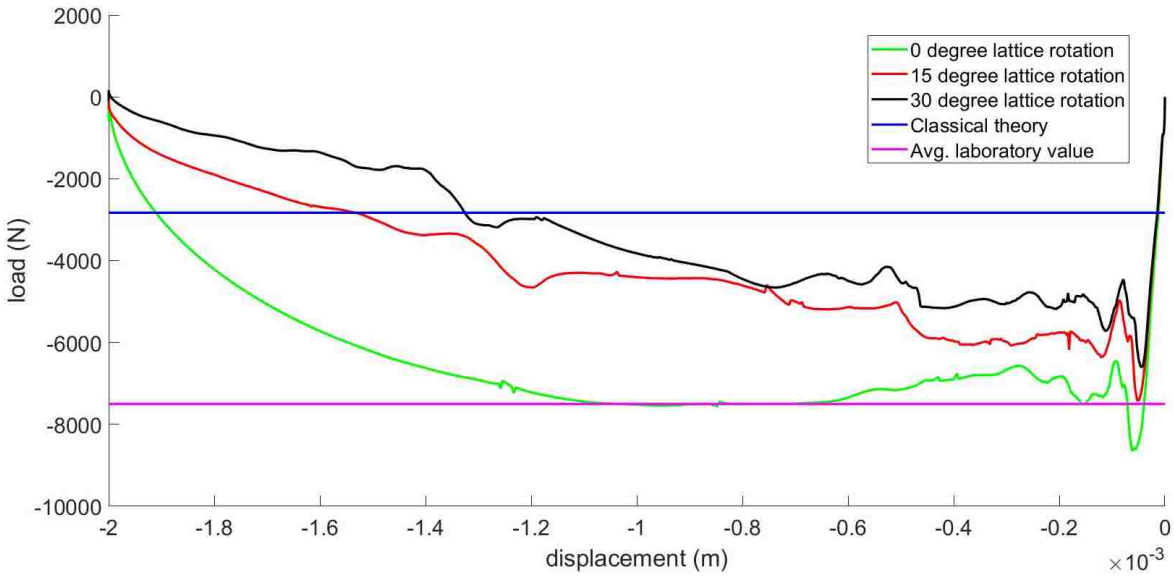

Figure 5-16 Load comparison between different lattice rotations, laboratory value and theoretical value for modulus of rupture test

5.5 Direct Compression test using SPLM

Let us now consider the compression specimen. The cylinder dimension is L*B*H (12” *6” *6”). We apply the compressive force to the top region of the specimen as the displacement. The bottom region is fixed. From the Fig. 5-17, we can see that in the compression simulation, more particles are damaged, and all the particles become plastic except the particles defined at the boundary. The plastic particle is shown by black color. We can see that the rotation of lattice does not have much effect on the load as seen in table 8. The lattice rotation of 0, 15 and 30 degrees have 605, 595 and 569 particles with the same number of time step i.e. 4600.

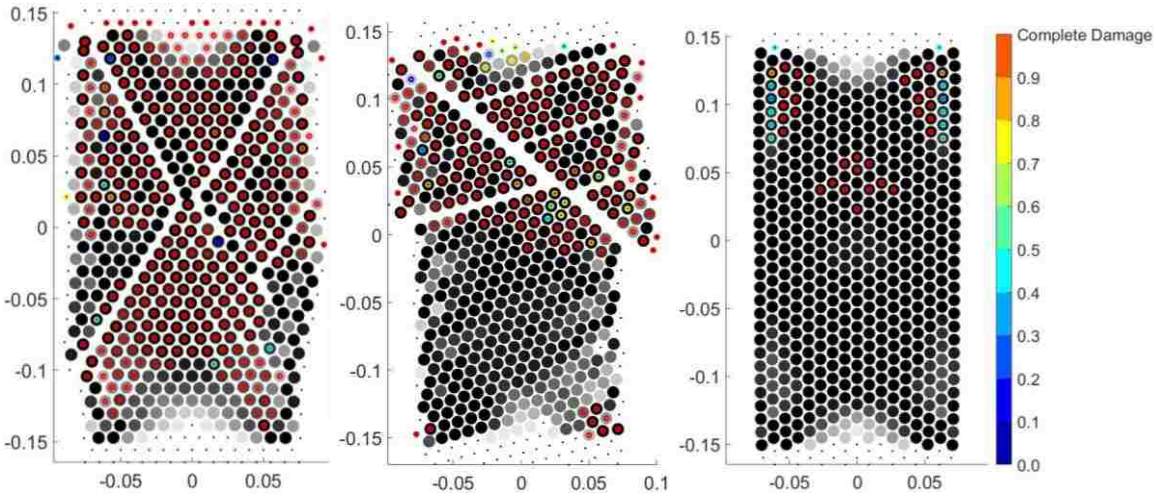

Figure 5-17 Cracking patterns obtained for direct compression test whose particle lattice is rotated through a)0, b)15 and c)30 degrees

The relation of force with displacement and time and displacement with time is shown in the graph in Fig. 5-18. The theoretical and the laboratory loads are again multiplied by the ratio of the cross-section area to obtain the loads for same specimen and the comparison is shown in the Fig. 5-19.

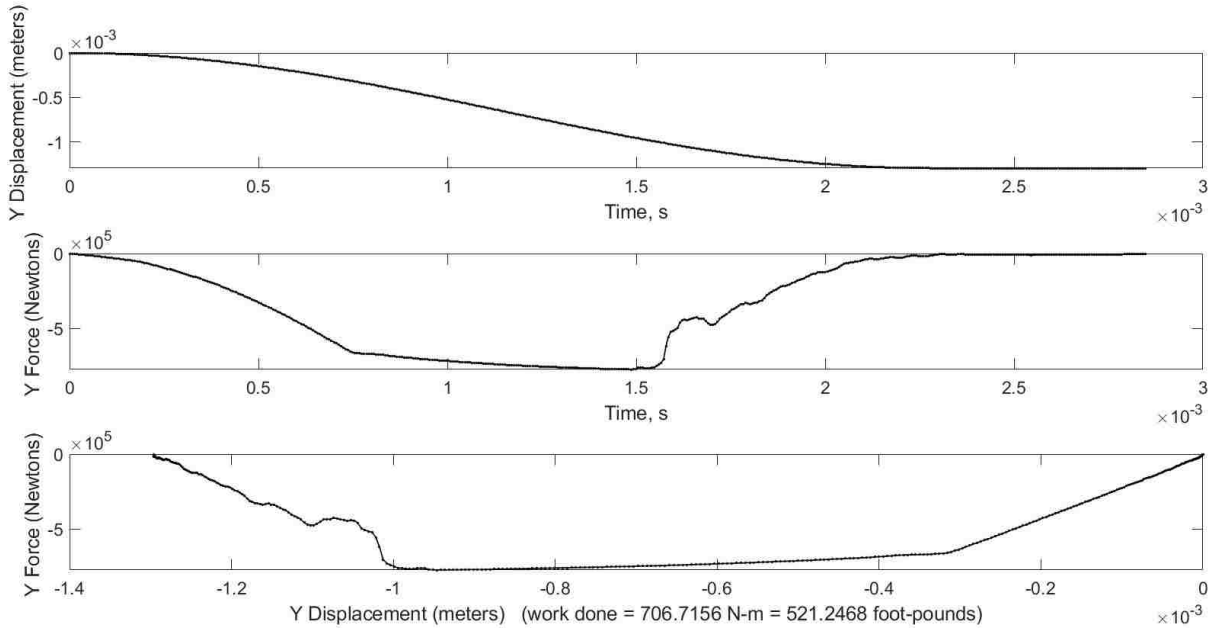

Figure 5-18 Plot of a) displacement vs time b) force vs time c) load vs displacement compressive strength specimen

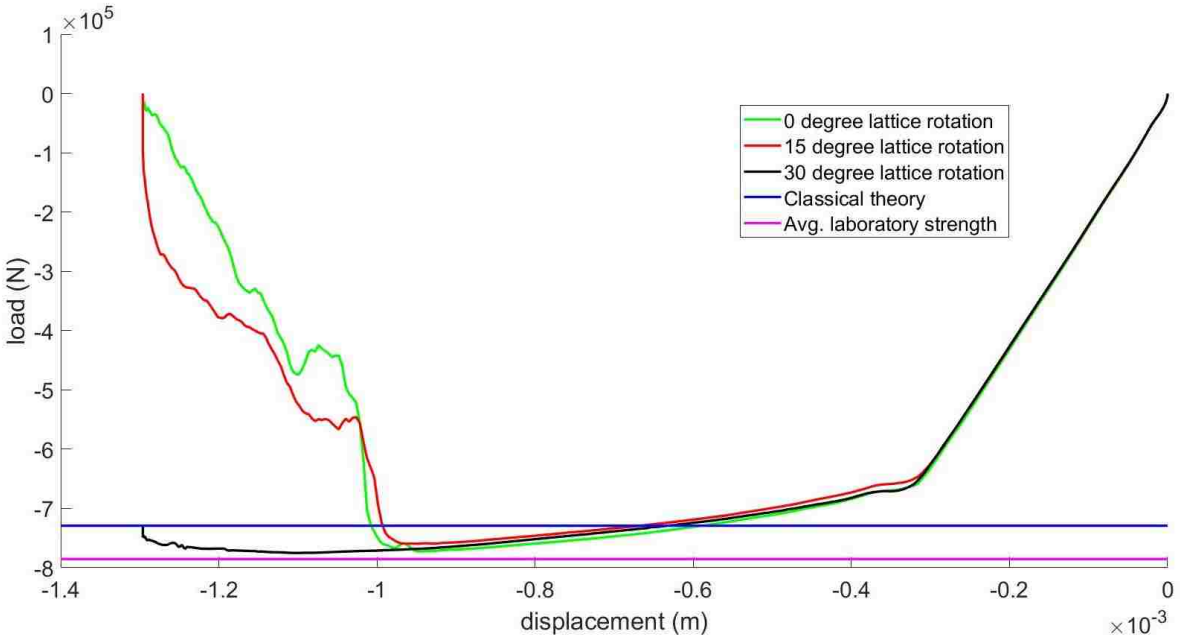

Figure 5-19 Load comparison between different lattice rotations, laboratory value and theoretical value for compressive strength test

5.6 Summary

After conducting the laboratory experiment and the SPLM simulation, the conclusion is drawn for the results of the peak load obtained from laboratory experiment. The results from SPLM simulation is summarized in Table 5-2.

Table 5-2 Comparison table for the results from Laboratory and SPLM

Types of SPLM Simulation	Peak Load, (N)			
	Brazilian Split Test	Direct Tension with bolt at center	Modulus of Rupture	Direct Compression
0° Lattice rotation	197100	37530	8626	772600
15° Lattice rotation	199400	37870	7424	758700
30° Lattice rotation	200400	41210	6594	775100
Average	198967	38870	7548	768800
Standard Deviation	1692	2034	1022	8836
Coefficient of Variation (%)	0.850	5.232	13.535	1.149

Average of SPLM Simulations	198967	38870	7548	768800
Average of Laboratory Results (Peak Load, N)	246337	42788	7503	785343
Difference (%)	21.276	9.596	0.598	2.129

The difference percentages are calculated as the ratio of difference of the SPLM simulation and the laboratory results to the averages of the SPLM simulation and laboratory results. The average laboratory results are then used in the formulas given by different ASTM standards to obtain the cracking strengths. The strengths are given by,

Splitting strength, $f_{sp} = \frac{2P}{\pi * L * D} = \frac{2*246337}{\pi*0.3048*0.1524} = 3.376$ MPa

Direct tensile test, $f_t = \frac{P}{A} = \frac{42788}{0.0225} = 1.9$ MPa

Modulus of rupture, $f_r = \frac{3 * P * L}{2 * b * d^2} = \frac{3*7503*0.3048}{2*0.0762*0.0762^2} = 7.75$ MPa

We then performed the linear regression analysis of the results obtained above. The regression analysis is performed for the three tensile tests, splitting strength (f_{sp}), direct tensile strength (f_t) and modulus of rupture (f_r) tests. We derive the relationship as mentioned below. For laboratory results, the relationship obtained for the cracking strength is

f_t / f_{sp} = 1.9 MPa/3.376 MPa = 0.56

f_t / f_r = 1.9 MPa/7.75 MPa = 0.25

f_{sp}/f_r = 3.376 MPa/7.75 MPa = 0.43

$f_r = 2.32\ f_{sp} = 4.0\ f_t$

Similarly, for the SPLM results,

f_t / f_{sp} = 1.73 MPa/2.73 MPa = 0.63

f_t / f_r = 1.73 MPa/7.8 MPa = 0.22

f_{sp}/f_r = 2.73 MPa/7.8 MPa = 0.35

For SPLM results, the relationship obtained for the cracking strength is

$f_r = 2.86\ f_{sp} = 4.54\ f_t$

From the above relationship, we can see that the regression value is higher for the results from SPLM than the laboratory experiment.

Chapter 6 Discussion and Conclusions

In this thesis, simulations of various laboratory tests using the SPLM have been presented. The SPLM model is rotated at various lattice rotation angles and spacings and the obtained results are compared with the laboratory test results. With SPLM, it is possible to model the problems of elasticity, plasticity, and damage based on discrete lattice particles. SPLM has the potential to model any material. Although SPLM is still in the development phase, it is already producing results that are comparable with the laboratory results. With future advancement, SPLM has the potential to be a competitive method with the continuum mechanics approach.

In SPLM the particles are arranged in lattice and they interact with other neighboring particles. The domain of the problem is not continuous. Hence, it can also be used to simulate the particle dynamic actions after the peak load has been attained. The SPLM simulation includes the time domain, which allows users to observe changes in the model during simulation.

The major advantage of peridynamics is in fracture mechanics where it allows damage and cracks to develop naturally. Despite the simplicity of SPLM, the simulations can produce results that can be used to study particle dynamics, elasticity, damage, and plasticity and the cracking patterns.

6.1 Discussion

In this thesis, we use 2D plane stress concrete simulations for validation. The laboratory results and the classical theory results are used to validate the SPLM results.

SPLM is computationally efficient and it addresses the damage and plasticity model in much easier way. The results obtained seem to be satisfactory and the SPLM may be used as an alternative method to classical continuum mechanics.

The SPLM simulations were conducted for different lattice rotations and it was observed that the pre-peak results for the same test were similar, but the cracking patterns varied.

The variance in the results were obtained in the SPLM simulation and the laboratory experiments. The conditions were not perfectly same for the tests which is why the variances are observed.

We can observe in the load comparison Figs. 5-6, 5-11, 5-16 and 5-19 in Chapter 5 that the SPLM simulation results are around or between the range of classical theory and the laboratory results. For Brazilian split cylinder test, the modulus of rupture test, and the compressive strength test we observed that the classical theory strength is lower than the laboratory and the SPLM simulation strengths. The classical theory strength is much lower for the modulus of rupture test which implies that the classical theory underpredicts the flexural strength. It assumes that when the initial crack occurs in the specimen, the specimen does not take any more load. However, we observed from the laboratory test and the SPLM simulation that the specimen can take load even after the initial crack forms (Fig. 4-11 a) & c)). The specimen undergoes strain-softening in concrete after the initial crack formation, however, it is still able to carry additional load. The ACI code 318-14

chapter 14, section 14.5.2.1 calculates the flexural strength at tension face to be $5\sqrt{(f'_c)}$ which is the strength at which the initial crack is formed, and the specimen can take more load until it finally, completely breaks.

The post peak behavior was also recorded during the laboratory test and the SPLM simulations. The post peak behavior can be unpredictable both in the laboratory and in the simulations. As we notice in Fig. 5-17 and Fig. 5-19 for compression test, the applied force does not go to zero after the specimen is damaged. The specimen retains some load after the peak and the particles remain intact in the specimen and do not separate. This phenomenon can be named "particle interlocking" which allows the specimen to carry some retained load before it completely breaks. This can be included in the future work.

6.2 Future Work

The validation results obtained from the SPLM simulations indicate that SPLM has potential to model damage and plasticity of concrete. It is also proposed that SPLM can model reinforced concrete with reasonable accuracy (Gerstle, 2015). It is desirable to use SPLM for the simulation of other materials like steel. The current SPLM model is able to output damage, plasticity and elasticity; however, it can also be developed to produce more advanced simulation results. The current version can only accommodate limited number of particles and the simulation time increases if the number of particles increase. Hence, it can be improved to incorporate more particles to refine the simulation results. It can be done either by increasing the horizon radius or decreasing the lattice spacing. SPLM is an excellent tool to study the fracture behavior in solid mechanics. SPLM also opens the possibilities of studying particle dynamics behavior during the crack formation which has been a topic of interest to many researchers.

References

ACI Committee 318, & American Concrete Institute. (2016). *Building code requirements for structural concrete (ACI 318-14): an ACI standard : commentary on building code requirements for structural concrete (ACI 318R-14), an ACI report*.

ASTM C136 / C136M-14, Standard Test Method for Sieve Analysis of Fine and Coarse Aggregates, ASTM International, West Conshohocken, PA, 2014, www.astm.org

Barenblatt, G. (1962). The Mathematical Theory of Equilibrium Cracks in Brittle Fracture. *Advances in Applied Mechanics Advances in Applied Mechanics Volume 7*,55-129. doi:10.1016/s0065-2156(08)70121-2

Bažant, Z. P., & Jirásek, M. (2002). Nonlocal Integral Formulations of Plasticity and Damage: Survey of Progress. *Journal of Engineering Mechanics*, *128*(11), 1119–1149. https://doi.org/10.1061/(ASCE)0733-9399(2002)128:11(1119)

Červenka, J., & Saouma, V. (1996). Discrete Crack Modeling in Concrete Structures. *Fracture mechanics of concrete structures*,*2*, 1285-1300.

Dugdale, D. S. (1960). Yielding of steel sheets containing slits. *Journal of the Mechanics and Physics of Solids*, *8*(2), 100–104. https://doi.org/10.1016/0022-5096(60)90013-2

Gerstle, W., Sau, N., & Silling, S. (2007). Micropolar peridynamic modeling of concrete structures. *Fracture mechanics of concrete and concrete structures*,*1*(1), 475-482.

Gerstle, Walter H., & Xie, M. (1992). FEM Modeling of Fictitious Crack Propagation in Concrete. *Journal of Engineering Mechanics*, *118*(2), 416–434. https://doi.org/10.1061/(ASCE)0733-9399(1992)118:2(416)

Gerstle, Walter Herbert. (2015). *Introduction to Practical Peridynamics: Computational Solid Mechanics Without Stress and Strain*. World Scientific Publishing Company.

Gerstle, W., Sau, N., & Silling, S. (2005). Peridynamic Modeling of Plain and Reinforced Concrete Structures. *18th International Conference on Structural Mechanics in Reactor Technology (SMiRT 18)*. Beijing, China:Atomic Energy Press.

Griffith, A. A. (1921). The Phenomena of Rupture and Flow in Solids. *Philosophical Transactions of the Royal Society A: Mathematical, Physical and Engineering Sciences*, *221*(582–593), 163–198. https://doi.org/10.1098/rsta.1921.0006

Gerstle, W., Sau, N., & Silling, S. (2007). Peridynamic modeling of concrete structures. *Nuclear Engineering and Design*,*237*(12-13), 1250-1258. doi:10.1016/j.nucengdes.2006.10.002

Hillerborg, A., Modéer, M., & Petersson, P.-E. (1976). Analysis of crack formation and crack growth in concrete by means of fracture mechanics and finite elements. *Cement and Concrete Research*, *6*(6), 773–781. https://doi.org/10.1016/0008-8846(76)90007-7

Honarvar, H., Gerstle, W., & Asadollahi, A. (2013). Computational simulation of reinforced concrete using the micropolar peridynamic lattice model. *VIII International Conference on Fracture Mechanics of Concrete and Concrete Structures.* FRAMCOS-8.

Inglis, C. (1913). Stresses in a plate due to the presence of cracks and sharp corners. *Transactions of the Institute of Naval Architects*, *55*, 219–242.

Ingraffea, A., Gerstle, W., Gergely, P., & Saouma, V. (april 01, 1984). Fracture Mechanics of Bond in Reinforced Concrete. *Journal of Structural Engineering*,*110*(4). doi:https://doi.org/10.1061/(ASCE)0733-9445(1984)110:4(871).

Khraisi, T. A., & Shen, Y. L. (2012). Introductory Continuum Mechanics with applications to Elasticity. https://stavfoydedli1970.files.wordpress.com/2018/07/17202959.pdf

Koenemann, F. (2014). Cauchy's stress theory in a modern light. *European Journal of Physics*, *35*, 5010. https://doi.org/10.1088/0143-0807/35/1/015010

Mase, G. T., & Mase, G. E. (1999). *Continuum mechanics for engineers* (2nd ed). Boca Raton, Fla: CRC Press.

Nikravesh, S., & Gerstle, W. (2018). Improved State-Based Peridynamic Lattice Model Including Elasticity, Plasticity and Damage. *Computer Modeling in Engineering & Sciences*, *116*(3), 323–347. https://doi.org/10.31614/cmes.2018.04099

Raphael, J. M. (1984). Tensile Strength of Concrete, ACI Journal, vol. 81, no. 2, pp. 158–165.

Shabazpanahi, S., Ali, A. A. A., Aznieta, F. N., Kamgar, A., & Farzadnia, N. (2012). A simple method to model crack propagation in concrete, (1), 10.

Silling, S. A. (2000). Reformulation of elasticity theory for discontinuities and long-range forces. *J. Mech. Phys. Solids*, 35.

Silling, S. A., Epton, M., Weckner, O., Xu, J., & Askari, E. (2007). Peridynamic States and Constitutive Modeling. *Journal of Elasticity*, *88*(2), 151–184. https://doi.org/10.1007/s10659-007-9125-1

Wittel, F.K., Kun, F., & Herrmann, H.J. 1 Particle models : Simulation of damage and fracture in composites using a discrete element approach.

Wosatko, A., Winnicki, A., & Pamin, J. (2011). Numerical analysis of Brazilian split test on concrete cylinder. *Computers & Concrete*, *8*(3), 243–278. https://doi.org/10.12989/cac.2011.8.3.243